Chemical Science

ROYAL SOCIETY OF CHEMISTRY

REVIEW

View Article Online
View Journal | View Issue

Cite this: *Chem. Sci.*, 2023, **14**, 2776

Advanced hematite nanomaterials for newly emerging applications

Hao Wan, [a] Linfeng Hu, [b] Xiaohe Liu, *[ac] Ying Zhang,*[a] Gen Chen,[c] Ning Zhang [c] and Renzhi Ma *[d]

Received 11th January 2023
Accepted 20th February 2023

DOI: 10.1039/d3sc00180f

rsc.li/chemical-science

Because of the combined merits of rich physicochemical properties, abundance, low toxicity, *etc.*, hematite (α-Fe_2O_3), one of the most chemically stable compounds based on the transition metal element iron, is endowed with multifunctionalities and has steadily been a research hotspot for decades. Very recently, advanced α-Fe_2O_3 materials have also been developed for applications in some cutting-edge fields. To reflect this trend, the latest progress in developing α-Fe_2O_3 materials for newly emerging applications is reviewed with a particular focus on the relationship between composition/nanostructure-induced electronic structure modulation and practical performance. Moreover, perspectives on the critical challenges as well as opportunities for future development of diverse functionalities are also discussed. We believe that this timely review will not only stimulate further increasing interest in α-Fe_2O_3 materials but also provide a profound understanding and insight into the rational design of other materials based on transition metal elements for various applications.

1. Introduction

The design and preparation of low-cost and high-performance materials are considered to be the critical aspects for expanding or creating applications in various fields ranging from optics and magnetics to electronics, biological medicine, *etc.*[1–3] To accelerate the progress of society as well as the boom of both science and technology, it is of great significance to develop new materials and/or explore the existing counterparts with other emerging functionalities or unprecedented applications.

Due to the combined advantages including rich abundance, low cost, and diverse species (metals/alloys, compounds and their composites) as well as praiseworthy physicochemical

[a]*Zhongyuan Critical Metals Laboratory, School of Chemical Engineering, Zhengzhou University, Zhengzhou, 450001, PR China. E-mail: liuxh@csu.edu.cn; zhangying777@zzu.edu.cn*

[b]*School of Materials Science and Engineering, Southeast University, Nanjing 211189, P. R. China*

[c]*School of Materials Science and Engineering, Central South University, Changsha, 410083, PR China*

[d]*International Center for Materials Nanoarchitectonics (WPI-MANA), National Institute for Materials Science (NIMS), Namiki 1-1, Tsukuba, Ibaraki, 305-0044, Japan. E-mail: MA.Renzhi@nims.go.jp*

Hao Wan is an assistant professor of the School of Chemical Engineering at Zhengzhou University. He received his B.S. (2013) and PhD (2019) from Central South University. From September 2016 to September 2018, he studied as an exchange student at the National Institute for Materials Science (NIMS) in Japan. His recent research interests include the design and synthesis of advanced nanostructures for electrochemical energy storage and conversion.

Xiaohe Liu is a professor at the School of Chemical Engineering, Zhengzhou University. He obtained his PhD degree at Central South University in 2005 supervised by Prof. Guanzhou Qiu, an academician of the Chinese Academy of Engineering. From September 2002 to September 2020, he worked for Central South University. Since October 2020, he has been a staff of Zhengzhou University. His research interests include the functionalization and engineering of layered materials and mineral materials.

characteristics originating from the magical d electron configurations, functional materials based on transition metal elements have attracted extensive research interest.[4–10] Among them, α-Fe_2O_3 with iron as the second most abundant metal element in the crust possesses the advantages of chemical stability,[11,12] redox activities,[13] low toxicity and cost,[14] *etc.*, and has been systematically studied for decades and widely applied in diverse fields including secondary batteries,[15,16] supercapacitors,[17] Fenton-like catalysts,[18] adsorbents,[19] photochemical oxidation reactions,[20,21] magnetics,[22] water–gas shift reaction,[23] and elevated-temperature CO oxidation.[24] On the other hand, certain shortcomings, such as unsatisfactory electroconductivity and relatively inert redox properties originating from the chemical stability, still exist for a typical α-Fe_2O_3 phase, hindering further widespread applications.[25,26] To overcome these intrinsic drawbacks, numerous efforts have been paid to the electronic structure modulation of α-Fe_2O_3 materials through nanostructure/composition design, such as those with large surface area, active facet exposure, and/or multicomponents, for optimizing the physicochemical properties and thus improving the performance in practical applications. For instance, Mao *et al.* reported that constructing hierarchical α-Fe_2O_3 nanospheres with hollow interiors could not only efficiently enhance electroconductivity but also tailor the properties of Li^+ ion storage, achieving satisfactory long-term cycling stability of retaining a reversible capacity of 965 mA h g^{-1} beyond 200 cycles.[27] Such a high capacity for Li-ion storage was far superior to that of the commercial graphite material with the theoretical value of 372 mA h g^{-1}.[28] As shown in Fig. 1a, in the past decade, publications concentrating on α-Fe_2O_3 presented a steadily increasing trend, which also implied that the associated materials have always been a research hotspot. Additionally, in very recent years, because of the rich physicochemical properties and/or multifunctionalities, α-Fe_2O_3 materials were also demonstrated to show significant breakthroughs in some frontier applications/fields including but not limited to electrocatalysis,[29,30] photocatalytic carbon dioxide (CO_2) reduction,[31] some specific photoelectrochemistry reactions,[32] chemical sensing,[33] and biological medicine (Fig. 1b).[34] These critical developments make α-Fe_2O_3 materials a promising competitor in these emerging fields.

To date, there are some excellent review reports on α-Fe_2O_3 materials focusing on their applications in contaminant removal, photoelectrochemistry and/or photocatalysis, *etc.*[35–39] Nevertheless, few of them have been dedicated to the newly emerging applications as mentioned above. Through carefully tuning the electronic structure by composition optimization and/or nanostructure design, α-Fe_2O_3 materials were demonstrated to show significant breakthroughs in these fields. It is, therefore, of great importance to timely review the recent progress in functional α-Fe_2O_3 materials for extended applications. In this work, we first offered/presented a brief introduction to the basic physicochemical features of α-Fe_2O_3 materials. The strategies toward careful design and construction of α-Fe_2O_3 materials with elaborate nanostructures/compositions were then summarized. In the following section, several cutting-edge applications of advanced α-Fe_2O_3 materials were systematically reviewed with a particular focus on the relationship between the composition/nanostructure-tailored electronic structure and practical performance. At last, a summary and perspectives on future orientations were provided. The understanding of the rationales and methodologies of α-Fe_2O_3 materials may also offer deep insights into both fundamental investigations and practical applications of other functional materials based on transition metal elements.

2. Basic structure and physicochemical properties

The crystalline α-Fe_2O_3 belongs to a conventional corundum (α-Al_2O_3)-like rhombohedral structure ($a = 5.036$ Å, $c = 13.750$ Å and $\gamma = 120°$ with the space group of $R\bar{3}c$),[40] in which a single

Ying Zhang is an assistant professor of the School of Chemical Engineering at Zhengzhou University. He received his B.E. (2009) and PhD (2019) from the Central South University (China). He studied as a visiting researcher from 2017 to 2019 at the University of California San Diego (United States). Currently, his research focuses on natural resource-derived nanostructures for energy storage and environmental applications.

Renzhi Ma is a group leader at the International Center for Materials Nanoarchitectonics (WPI-MANA), National Institute for Materials Science (NIMS), and a guest professor at the Department of Nanoscience and Nanoengineering, Faculty of Science and Engineering, Waseda University, Japan. He also serves as an Associate Editor of Royal Society of Chemistry (UK) journals Nanoscale & Nanoscale Advances. He received his BE and PhD from Tsinghua University (Beijing, China). Since 2000, he has worked at NIMS. His recent research interests include developing advanced functional 1D/2D nanomaterials and hybrids for energy-related applications.

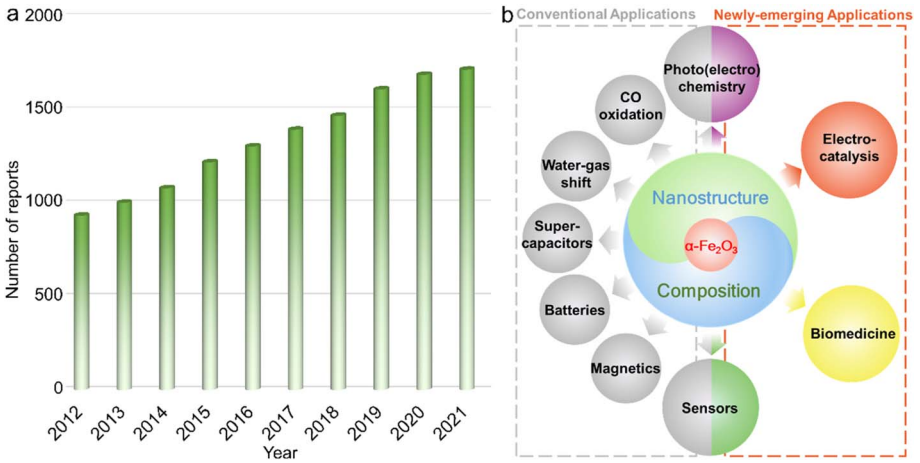

Fig. 1 Development trend of multifunctional α-Fe_2O_3 materials. (a) The time-dependent histogram of the publications associated with α-Fe_2O_3 materials in the past decade (data from the Web of Science Core Collection). (b) Application fields of α-Fe_2O_3 materials.

unit consists of alternately arranged Fe and O atom layers, and all the Fe atoms are in [FeO_6] coordination with the chemical valence of +3, as displayed in Fig. 2a. Because of the half-occupied 3d electronic structure of Fe^{3+} ions, *i.e.*, [Ar]$3d^5$, the α-Fe_2O_3 phase is rather stable even under elevated-temperature conditions and/or in aqueous solution (pH > 3).[41–43] Moreover, this half-occupied electron configuration also causes a relatively large magnetic moment, such as ~5.0 μ_B for Fe^{3+} ions in a high-spin state.[44] However, the adjacent Fe^{3+} ion planes in [111] orientation, separated by O^{2-} ion layers, are in an antiparallel arrangement below the Morin temperature (T_M, ~260 K for the bulk structure), resulting in antiferromagnetism. In contrast, as

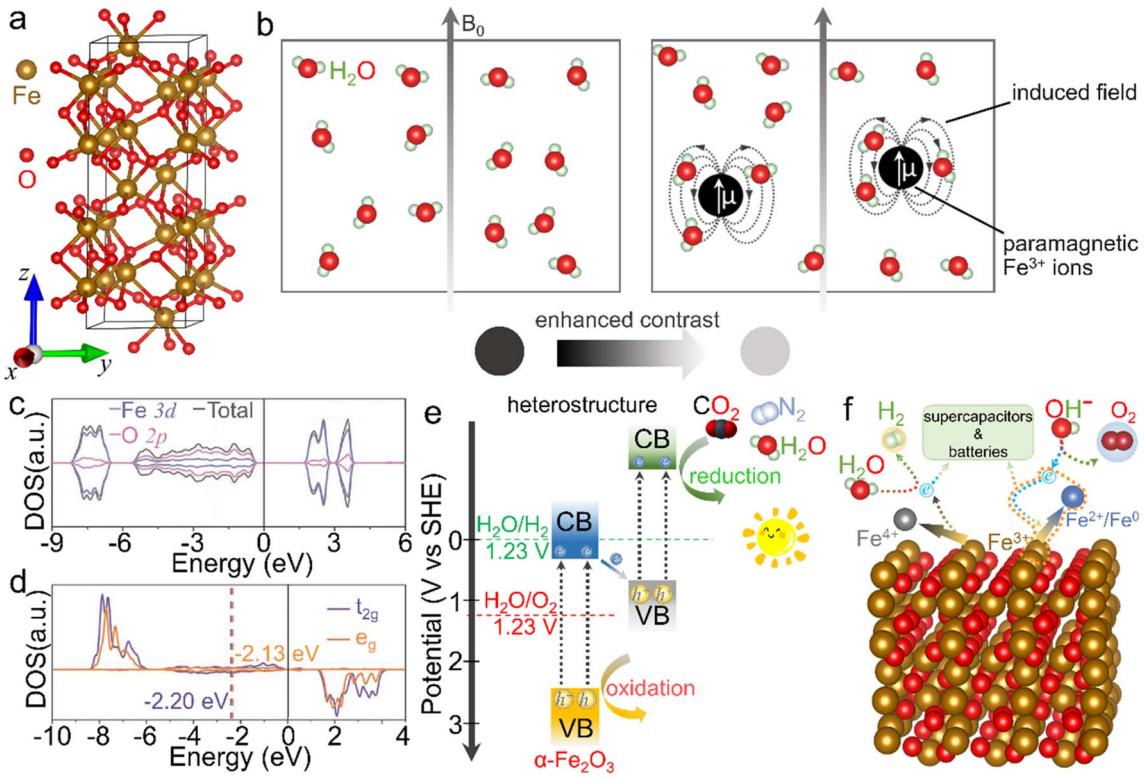

Fig. 2 Crystal structure and basic physicochemical characteristics of the α-Fe_2O_3 phase. (a) Crystal structure of the rhombohedral α-Fe_2O_3 phase, in which brown and red balls represent iron and oxygen atoms, respectively. (b) Scheme for the enhanced T_1-weighted magnetic resonance contrast induced by paramagnetic ions, wherein B_0 represents an external field. (c) Density of states (DOS) and (d) projected DOS on the spin orbitals of t_{2g} and e_g of Fe atoms. (c and d) Adapted with permission from ref. 54. Copyright 2019, John Wiley & Sons, Inc. (e) Scheme of an α-Fe_2O_3-based heterostructure for photocatalysis. (f) Scheme for the redox properties of α-Fe_2O_3 for energy-related applications.

the ambient temperature increases above T_M, α-Fe_2O_3 serves as a paramagnet because of the slightly canted-spin Fe^{3+} ions.[45–47] Such an interesting magnetic behavior can also be considerably tailored by the electronic structure through morphology design and composition tuning. For example, Velev *et al.* proposed that 3d transition metal ion dopants (such as Sc^{3+} and Ga^{3+} cations) in the α-Fe_2O_3 lattice could enormously modulate the location of d states and thus the net magnetic moments.[48] Besides, similar to the widely known Gd^{3+} with a $4f^7$ electron structure and Mn^{2+} with a $3d^5$ counterpart, the half-occupied 3d configuration also makes Fe^{3+} ions themselves highly paramagnetic.[49–51] As shown in Fig. 2b, when water molecules move into the regions of the induced dipole moment of paramagnetic Fe^{3+} ions, the relaxation process of protons in the water is disturbed and thus the longitudinal spin-lattice relaxation time is shortened, leading to the enhanced T_1-weighted contrast effect. However, α-Fe_2O_3 shows a dissatisfactory contrast effect in practical application due to the above-mentioned atomic arrangement.

On the other hand, α-Fe_2O_3, a typical n-type semiconductor with a bandgap of ~2.0 eV, is also a potential visible-light-driven photocatalytic material.[52,53] Fig. 2c and d shows a d band center of −1.88 eV, while a small crystal-field splitting of 0.07 eV between the t_{2g} and e_g center values indicates the intrinsic high-spin state and total spin polarization of Fe^{3+} ions.[54] In view of the bandgap as well as valence band location, α-Fe_2O_3 can absorb and utilize both ultraviolet light and partial visible light, serving as an extensively studied catalyst in photochemical reactions such as dye degradation and water oxidation.[55] However, it generally suffers from the drawbacks of poor conductivity and fast recombination of photo-induced electron–hole pairs, due to which the inherent photocatalytic activity is mediocre and needs to be further improved.[56] More importantly, the conduction band position is much higher than the theoretical values of many reduction processes, such as hydrogen evolution, carbon dioxide reduction reaction and nitrogen reduction reaction. To trigger these photocatalytic energy-related reduction reactions, it is indispensable to combine α-Fe_2O_3 with other semiconductors of proper electronic band structures to construct composites (*e.g.*, type-II heterostructures), as depicted in Fig. 2e. In this case, the oxidation reaction and reduction process may concurrently occur over these α-Fe_2O_3 composites. In addition, Fe^{3+} ions in α-Fe_2O_3 materials are in the intermediate oxidation state. In other words, they can be further oxidized into Fe(IV) and/or reduced to Fe(II)/Fe(0) species under suitable external conditions.[57–60] The redox activity makes it feasible in energy-related fields (Fig. 2f). When it comes to energy storage application, α-Fe_2O_3 delivers a large specific capacitance of 3265 F g^{-1} theoretically as an active electrode material for supercapacitors in the voltage window of −1.0 to 0 V.[61] Recently, redox characteristics, which exhibited activity in some newly emerging applications such as electrocatalysis, photoelectrochemistry and environmental fields, *etc.*, have also been investigated, extending the functionality of α-Fe_2O_3 materials. On account of these basic physicochemical properties, α-Fe_2O_3 is greatly cherished as a promising material with multifunctionalities. To further optimize the physicochemical properties and thus improve the practical performance in various applications, many efforts have been paid to the modulation of the electronic structure through the elaborately designed nanostructures and compositions, which will be introduced below.

3. Preparation of α-Fe_2O_3 materials

It is generally accepted that morphology and composition are the two dominant factors governing the electronic structures of functional materials and thereby tuning the physicochemical properties as well as improving the practical performance in a variety of applications. After several decades of attempts, α-Fe_2O_3 materials with exquisite nanoarchitectures and/or carefully designed compositions have been synthesized.

3.1. Single-phase α-Fe_2O_3 materials

Reducing the size of α-Fe_2O_3 materials, *i.e.*, constructing nanostructures, is regarded as an efficient approach, giving rise to the combined advantages of larger specific surface area, increased active sites accessible, better electroconductivity, *etc.* Among various strategies for the preparation of single-phase α-Fe_2O_3 nanomaterials with specific composition/morphologies, solvothermal and/or hydrothermal methods using organic solvents/organic solvent-containing solution mixtures or pure water as the reaction system are the most popular.[62–64] The sealed reaction vessels can provide both relatively high temperature (*e.g.*, 180 °C) and pressure conditions, which give rise to the direct synthesis of α-Fe_2O_3 materials, *i.e.*, the chemical conversion of iron salts into oxides ($Fe^{3+} + 3OH^- \rightarrow FeOOH + H_2O$, $2FeOOH \rightarrow \alpha\text{-}Fe_2O_3 + H_2O$).[65,66] More importantly, the nanostructures prepared *via* solvothermal/hydrothermal methods are generally uniform in both size and morphology (see Table 1 for the detailed characteristics of the synthetic methods). Using a mixture of ethylene glycol and water as the reaction system of the solvothermal process, Chen *et al.* achieved the preparation of α-Fe_2O_3 nanodisks.[67] Compared with the pure water, this mixture exhibited a larger viscosity but also induced a lower environment pressure and slower hydrolysis of metal ions, which contributed to the controlled growth of α-Fe_2O_3 crystalline grains. Through adjusting the molar ratio of the reaction ingredients, *i.e.*, $Fe(NO_3)_3$ and KOH, the growth rate was efficiently tuned and thus the gradual size decrease of α-Fe_2O_3 nanodisks from 100 nm to 43 nm was realized. To further reduce the size, organics especially long-chain counterparts were generally adopted for the controlled growth of nanocrystals. For instance, using oleic acid ($CH_3(CH_2)_7CH{=}CH(CH_2)_7COOH$) as the capping agent in the solvothermal process, Yu's group prepared monodisperse α-Fe_2O_3 nanocrystals with a mean size of ~14.7 nm successfully.[68] Oleic acid was popularly adopted for the formation of nanocrystallites; however, it made the surface hydrophobic, which was not beneficial enough for the subsequent widespread applications.[69–71] Jiang *et al.* chose poly(vinyl pyrrolidone) (PVP) to cap the α-Fe_2O_3 grains during the hydrothermal process, ensuring that the nanocrystals were highly

Table 1 Two popular strategies for the preparation of α-Fe_2O_3 materials

Synthetic strategies	Advantages
Solvothermal/ hydrothermal methods	• One-pot synthesis (*i.e.* simplicity) • Relatively low reaction temperature (160–200 °C) • Products with a rather uniform size and morphology • Facile composition/nanostructure tuning through choosing various additives and reaction systems • Suitable for both α-Fe_2O_3 materials and their composites
Topochemical transformation strategies	• Various precursor species (such as Fe (oxy) hydroxides and MOFs) with delicate nanostructures • Tuneable crystalline through simply changing the calcination temperature • Easily constructed lattice defects and/ or porous nanostructures • Suitable for both α-Fe_2O_3 materials and their composites

hydrophilic and dispersed.[72] Nanostructures with hollow interiors, another favorable morphology optimizing the physicochemical properties of α-Fe_2O_3 materials, could also be created by one-pot solvothermal/hydrothermal processes. Li and co-workers used sodium phosphate monobasic (NaH_2PO_4) to build an acidic environment in the hydrothermal process, resulting in the fast dissociation of the Fe source (*i.e.*, $K_4Fe(CN)_6$) and thus the formation of hollow α-Fe_2O_3 nanospheres without any templates, as displayed in Fig. 3a.[73] Moreover, using soluble $FeCl_3$ and $NH_4H_2PO_4$ in the hydrothermal reaction, Nathan obtained a nanotubular α-Fe_2O_3 product.[74] Although these additives were widely used for the synthesis of hollow α-Fe_2O_3 nanostructures, other experimental parameters such as temperature and concentration were also crucial for morphology control.

In particular, among numerous single-phase α-Fe_2O_3 materials, uniform polyhedral counterparts with high-index facet exposure represent a special type. Generally, in conventional growth processes, crystals enclosed by low-index facets are more preferred thermodynamically. In contrast, high-index facets refer to the large atomic arrangement densities and rich unsaturated coordination environments,[75,76] which are favorable for the linkage with plenty of dangling bonds and thus applications such as catalysis, sensors, effluent treatment, *etc.* To obtain high-index facet-covered α-Fe_2O_3 polyhedra, extensive attempts on solvothermal/hydrothermal processes using different synthetic systems and/or additives have been made to control the preferred orientation during the crystal growth process. Fig. 3b shows α-Fe_2O_3 pseudocubes bearing exclusively {012} facets, which were prepared in a solvothermal reaction system of ethanol with the co-presence of long-chain sodium oleate and oleic acid molecules.[77] This approach was similar to that reported by Yu *et al.*[68] However, through merely tuning the sodium oleate/$FeCl_3$ feed ratio (where $FeCl_3$ acted as the iron source), angular pseudocubes were created. Wu and co-workers reported {104} facet-enclosed rhombohedra using a mixed formamide–water system in the solvothermal process, as depicted in Fig. 3c.[78] Compared with water, the much more viscous reaction system could slow down the crystal growth, favorable for the formation of high-index facets. Fig. 3d displays the TEM image of α-Fe_2O_3 nanorods with {110} facets dominantly, which were prepared in pure 1,2-diaminopropane solution with the absence of water under solvothermal conditions.[79] Apart from these organic systems/additives, inorganic counterparts were also reported for the efficient control of crystal growth. Fig. 3e and its inset show elongated α-Fe_2O_3 icositetrahedra which were obtained in an aqueous $H_2PO_4^-$ solution of high concentration. Li *et al.* also demonstrated that the aspect ratio of the icositetrahedral product could be readily tuned by adjusting the $H_2PO_4^-$ concentration.[80] Moreover, Patra and co-workers unveiled that the hydrothermal temperature of an aqueous sodium salicylate–NaOH system was also a crucial factor for the exposure of distinct surface facets.[81] Stimulated by the fact that the common synthetic strategies employed environmentally harmful additives or complicated reaction systems to trigger the exposure of high-index/activity facets, our team proposed adding benign acetates (Ac^-) in the solvothermal process.[82] As shown in Fig. 3f–n, through simply tuning the Ac species as KAc, NaAc and NH_4Ac, respectively, uniform truncated bipyramid-, pseudocube- and plate-like nanoparticles with different surfaces were prepared. The morphological distinctions implied that the exposed facets could also be regulated by the inorganic cation species in synthetic systems. Furthermore, Zhi's group disclosed a facet controlling reagent-free route in which $FeCl_3$ solution served as the exclusive starting material.[83] Under hydrothermal conditions assisted by high-energy microwaves for only 30 min, truncated bipyramid nanoparticles with the exposure of twelve equivalent high-index $\{2\bar{1}5\}$ facets were synthesized, as indicated in Fig. 3o. This convenient procedure offers a promising additive-free strategy for the rapid preparation of advanced α-Fe_2O_3 materials; nevertheless, it requires some specific synthetic conditions such as high-energy microwave assistance, which may limit the widespread studies on novel synthetic strategies. Besides the morphology control, composition tuning can also be facilely realized through solvothermal/hydrothermal processes. For instance, to further amplify the property superiorities, dopants including metal ions (such as Co^{2+}) and/or non-metal guests (*e.g.*, F^-) have been introduced into the α-Fe_2O_3 host lattices, as displayed in Fig. 3p and q, respectively.[84,85]

For the preparation of some delicate nanostructures, carefully designed two- and/or multi-step strategies have also been developed. Among them, nanoarrays anchored on conductive substrates, widely used as working electrodes in the photo(-electro)chemistry field, were commonly attained through calcining the precursors which were obtained *via* electrochemical anodization approaches or hydrothermal/solvothermal processes.[86] In the calcination process, a relatively high temperature, such as 550 °C, is generally indispensable for the thermal-conversion/pyrolysis of the precursors. Similar topochemical transformation strategies were also

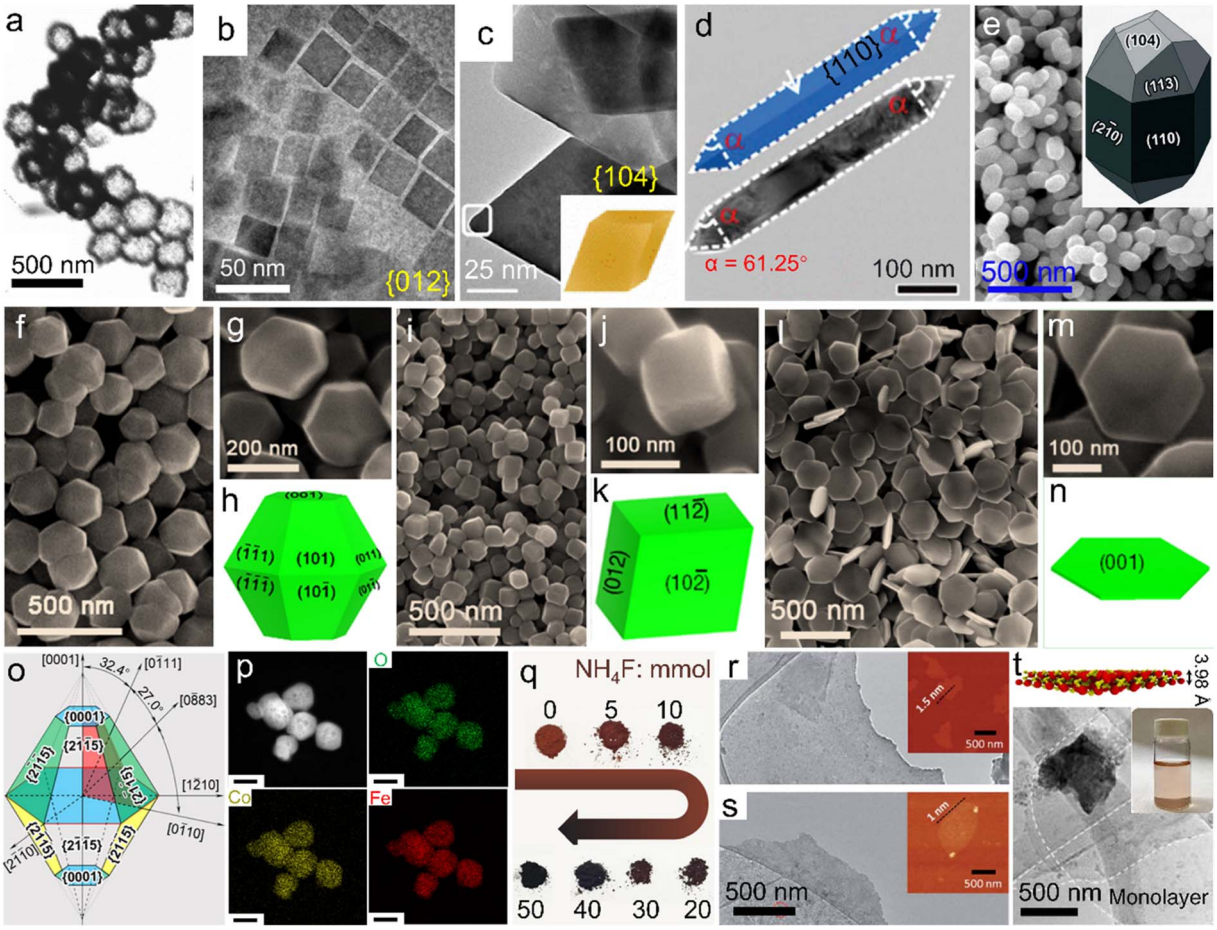

Fig. 3 Single-phase α-Fe_2O_3 materials with different compositions and/or morphologies. (a) Hollow nanospheres. Adapted with permission from ref. 73. Copyright 2007, American Chemical Society. (b) Nanocubes. Adapted with permission from ref. 77. Copyright 2019, American Chemical Society. (c) Pseudocubes. Adapted with permission from ref. 78. Copyright 2018, American Chemical Society. (d) Nanorods. Adapted with permission from ref. 79. Copyright 2018, Royal Society of Chemistry. (e) Icositetrahedra. Adapted with permission from ref. 80. Copyright 2015, Royal Society of Chemistry. Uniform polyhedra prepared using (f–h) KAc, (i–k) NH_4Ac and (l–n) NaAc. (f–n) Adapted with permission from ref. 82. Copyright 2016, Royal Society of Chemistry. (o) Truncated bipyramid nanoparticles. Adapted with permission from ref. 83. Copyright 2016, American Chemical Society. (p) Co-doped α-Fe_2O_3 nanoparticles. Adapted with permission from ref. 85. Copyright 2022, Elsevier Inc. (q) F-doped products with different doping ratios. Adapted with permission from ref. 84. Copyright 2017, John Wiley & Sons, Inc. (r) FeOOH nanosheets and (s) the corresponding calcined product. (r and s) Adapted with permission from ref. 87. Copyright 2020, Royal Society of Chemistry. (t) Crystal structure model and TEM image of as-exfoliated hematene monolayers. Adapted with permission from ref. 91. Copyright 2018, Nature Publishing Group.

reported for the preparation of α-Fe_2O_3 from other delicate nanostructures and/or precursor species. As an example, ultrathin nanosheets (~1.0 nm in thickness) were synthesized through the calcination at 500 °C of a sheet-like ferric oxyhydroxide (FeOOH) precursor, which was prepared through the deposition of inorganic salts on rock salt crystals (Fig. 3r and s).[87] It should be noted that during high-temperature calcination procedures for the formation of α-Fe_2O_3 crystals under some specific atmospheres, rich lattice defects can be facilely constructed, which may also be beneficial for the modulation of the electronic structure. Tong's group further adopted a nitrogen atmosphere for the calcination of FeOOH nanorods, gaining oxygen-deficient α-Fe_2O_3 counterparts.[88] Besides, organic precursors such as metal–organic frameworks (*e.g.*, MIL-88A) were also adopted for the preparation of porous α-Fe_2O_3 nanostructures through calcination in air.[89] It should be noted that the doping of guest ions into α-Fe_2O_3 lattices can also be achieved by the topochemical transformation strategies. Apriandanu *et al.* successfully prepared Ti-doped α-Fe_2O_3 nanoparticles through calcining the hydrothermal precursor, *i.e.*, Ti-containing Fe (oxy)hydroxide, at different temperatures. In this case, the crystallinity tuning was simultaneously achieved.[90]

Furthermore, very recently, Balan demonstrated that through the ultrasonic exfoliation of bulk α-Fe_2O_3 powder in *N*,*N*-dimethylformamide, hematene monolayers with a theoretical thickness of 3.98 Å were obtained, as displayed in Fig. 3t.[91] These nanosheets may provide an ideal platform for assembling them with other two-dimensional (2D) or 2D-like fundamental building blocks for the construction of functional materials.

3.2. α-Fe_2O_3 composites

Besides the doped single-phase materials, composites referring to the integration of α-Fe_2O_3 with one or more fundamental materials stand for another efficient way of composition tuning for electronic structure modulation. In addition to inheriting the physicochemical features from the maternal substances, some unexpected properties associated with the synergetic effects and/or interfacial electron interactions may also generate. For the preparation of the designed α-Fe_2O_3 composites, several typical synthetic strategies have been widely adopted. We have demonstrated a one-pot solvothermal approach using graphene oxide and Fe^{3+} salt as the starting materials for the direct preparation of the α-Fe_2O_3/reduced graphene oxide (simplified as α-Fe_2O_3/rGO) product. Since the graphene oxide nanosheets obtained by the Hummers' method were negatively charged, they could tightly combine with Fe^{3+} ions based on electrostatic interactions. Oxide nanoplates were thus *in situ* formed under a relatively-temperature solvothermal condition and wrapped by rGO nanosheets, as indicated in Fig. 4a.[92] Similar adsorption pre-treatments have also been used for other solvothermal/hydrothermal/reflux precursors, which can be further transformed into α-Fe_2O_3 composites through topochemical synthetic processes. Fig. 4b shows an α-Fe_2O_3/carbon nanotube composite (α-Fe_2O_3/CNTs), which was obtained through a reflux process using Fe^{2+} and CNTs as the feeds and a subsequent high-temperature calcination procedure of the reflux product (*i.e.*, FeOOH/CNTs precursor) at 700 °C.[93] Likewise, negatively charged Ti_3C_2 MXene nanosheets could also combine with Fe^{3+} ions. Through a hydrothermal process at a relatively low temperature (*e.g.*, 100 °C) for the *in situ* formation of FeOOH, the precursor FeOOH/Ti_3C_2 composite was constructed and topochemically transformed into the α-Fe_2O_3/TiO_2 hybrid after an annealing process with O_2 flow, as displayed in Fig. 4c.[94] Through the *in situ growth of* oxide and/or its precursors (such as FeOOH) on the supports, α-Fe_2O_3 was tightly combined with other fundamental phases, which might contribute to the more electronic interactions and thus promoted the electron transfer and was beneficial for the catalytic processes. Besides, the *in situ growth* of precursors in liquid systems may also effectively improve the homogeneity of the composites. Recently, carbonaceous organic precursors, such as Fe-MOFs, have also been demonstrated for the preparation of α-Fe_2O_3/C composites through the topochemical transformation strategies (*i.e.*, high-temperature calcination).[95,96]

Also, α-Fe_2O_3 could be employed as a substrate material supporting other active materials (*e.g.*, Pt nanoparticles) for the construction of the composites, referring to the as-called post-synthesis strategies.[97,98] Through the *in situ* reduction of platinum precursors (*e.g.*, $H_2PtCl_6 \cdot 6H_2O$) on the α-Fe_2O_3 substrate with the assistance of relatively elevated temperature of viscous organic solvents such as ethylene glycol, the size of Pt nanocrystallites could be facilely controlled and concurrently the agglomeration issue of the catalysis-active component, *i.e.*, Pt, was effectively alleviated, as depicted in Fig. 4d.[99] Further

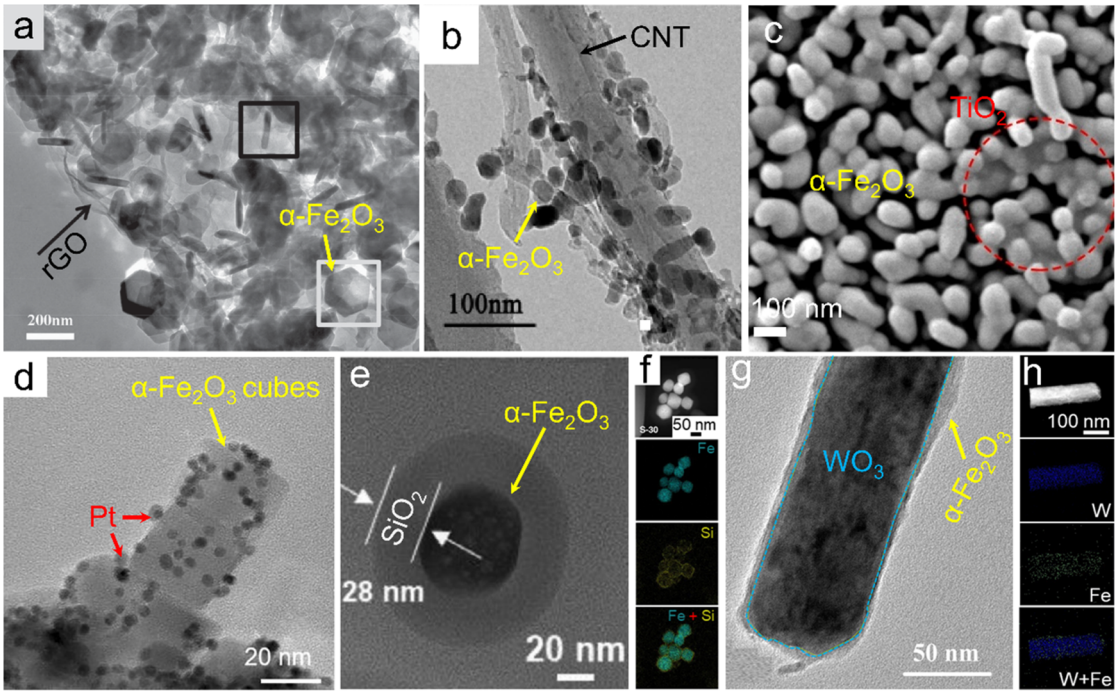

Fig. 4 α-Fe_2O_3 composites. (a) α-Fe_2O_3/rGO. Adapted with permission from ref. 92. Copyright 2014, John Wiley & Sons, Inc. (b) α-Fe_2O_3/CNTs. Adapted with permission from ref. 93. Copyright 2018, Elsevier Inc. (c) α-Fe_2O_3/TiO_2 composites. Adapted with permission from ref. 94. Copyright 2021, Elsevier Inc. (d) Pt-loaded α-Fe_2O_3 nanocubes. Adapted with permission from ref. 99. Copyright 2021, Elsevier Inc. (e and f) α-Fe_2O_3@SiO_2 core@shell. Adapted with permission from ref. 101. Copyright 2021, Elsevier Inc. (g and h) WO_3@α-Fe_2O_3 core@shell composite. Adapted with permission from ref. 102. Copyright 2019, John Wiley & Sons, Inc.

downsizing Pt nanoparticles to the extremely atomic scale, a Pt single atom-anchored α-Fe_2O_3 (denoted as Pt_1/α-Fe_2O_3) material was thereby obtained. Gao and co-workers adopted a photochemical deposition strategy in which a defined amount of $H_2PtCl_6 \cdot 6H_2O$ was added and slowly deposited in an Ar-saturated H_2O–methanol mixture under Xe irradiation for the construction of Pt single atoms on the α-Fe_2O_3 support.[100] In this case, Pt–Fe pair sites in the Pt_1/α-Fe_2O_3 catalyst possessed partially occupied orbitals due to the strong metal–support electronic coupling. Similarly, post-synthesis modifications were also reported for some other delicately nanostructured composites. A SiO_2 coating was formed through the hydrolysis of its precursor (*e.g.*, tetraethoxysilane) on the surface of α-Fe_2O_3 and thus α-Fe_2O_3@SiO_2 core@shell nanoparticles were generated, as indicated in Fig. 4e and f.[101] The thickness of the shell (*i.e.*, SiO_2 layer) was tunable with the molar ratio between the Si source and α-Fe_2O_3. On the other hand, the α-Fe_2O_3 component could also be designed on the surface of other fundamental materials for preparing the composites *via* the post-synthesis processes. Fig. 4g and h displays core@shell-like WO_3@α-Fe_2O_3 nanorods which were obtained through a spin coating strategy on the WO_3 core using an ethanol solution of $Fe(NO_3)_3$ as the feed and a following sintering process at 550 °C.[102] Furthermore, on account of the redox-active properties of Fe^{3+} ions, Fan *et al.* realized the preparation of a heterostructural α-Fe_2O_3/Fe_3O_4 catalyst *via* the partial reduction of the α-Fe_2O_3 counterpart by a carbonaceous support.[103] The post-synthesis modification strategies may be beneficial for the controlled exposure of active components and thus improve the practical applications, especially in the catalysis field.

Compared to the conventional doping strategies for tailoring the composition, component tuning by constructing composites based on α-Fe_2O_3 not only regulates the ratio of different fundamental phases randomly but also provides numerous possibilities for combining with kinds of other species including but not limited to elementary substances and compounds, which may provide a more facile approach for the optimization of the electronic structure and thus physicochemical properties.

4. Newly emerging applications

4.1. Electrocatalysis

With the steadily increasing global population and energy demands as well as severe environmental or even climatic issues, major concerns over future clean energy have been raised. Electrocatalysis using the inexhaustible substances in the air (*e.g.*, nitrogen and water) and reproducible electricity resource is highly evaluated for the sustainable synthesis of high-value-added fuels and/or chemicals under mild conditions, *i.e.*, ambient temperature and gas pressure. During these advanced energy conversion processes, electrocatalysts play a crucial role in determining the reaction rate, efficiency and selectivity. However, the state-of-the-art electrocatalysts are almost based on noble metal elements, for instance, RuO_2 and IrO_2 for the oxygen evolution reaction (OER) while the Pt/C composite for the hydrogen evolution reaction (HER).[104] Considering the high cost and scarcity of noble metal resources, developing much cheaper and more abundant candidates is persistently perused for the wide application of electrocatalysis.

4.1.1. Water splitting. Over the past few years, a mass of advanced α-Fe_2O_3 materials have arisen for diverse electrocatalytic reactions among which overall water splitting, composed of hydrogen and oxygen evolution half-reactions, has attracted a wide range of attention due to the clean combustion and relatively high energy density of hydrogen fuel. As a fact, the overall reaction was kinetically hindered by the sluggish oxygen evolution part. Generally, α-Fe_2O_3 itself showed a modest OER activity and further elaborate modifications were necessary. Riley *et al.* constructed Au nanostar and surface oxygen vacancy (V_O) co-decorated α-Fe_2O_3 (denoted as V_O-α-Fe_2O_3/Au) for the electrocatalytic OER, and found that the more V_O coverage made the d band center of Fe sites closer to the Fermi level and thus led to a less filled antibonding orbital, contributing to improved adsorption of intermediates. In addition, Au nanostars could efficiently improve the electroconductivity. As a result of the synergistic effect, V_O-α-Fe_2O_3/Au showed higher activity than both V_O-free α-Fe_2O_3/Au and bare α-Fe_2O_3 samples, as depicted in Fig. 5a–c.[105] Besides, the electronic structure was also facilely tuned by doping for activity enhancement. Xie and co-workers demonstrated that an appropriate F^- dopant in α-Fe_2O_3 nanoparticles could result in the generation of defect levels as well as the decreased band gap, enhancing the electrical conductivity. Moreover, the more electronegative F atoms than O counterparts increased the positive charges of the active Fe sites, facilitating the adsorption of OH^- and thus giving rise to more favorable kinetics.[84] Similarly, it was also demonstrated that metallic ions, such as Co^{2+} and non-redox Zn^{2+}, could markedly optimize the performance toward electrocatalytic water oxidation.[106,107] In addition to atomic substitution, high-index facet engineering was also verified as an efficient strategy for the improvement of OER activity. Fig. 5d–f present the OER activities of single-crystalline α-Fe_2O_3 nanoparticles exposed with different facets.[108] Higher current response (*i.e.*, 10 and 93.4 mA cm^{-2} at the potential of 1.55 and 1.65 V *vs.* RHE, respectively) and lower Tafel slope (51.8 mV dec^{-1}) in NaOH solution were detected for high-index (012) facets with oxygen termination (noted as (012)-O), suggesting the high activity and rapid reaction kinetics. Such an excellent activity was theoretically ascribed to the optimized adsorption/desorption properties for both the reactant and intermediates because of the electronic structure modulation, as supported by the Gibbs free energy change of each step. Analogous facet-dependent OER activities following the order of (001) > (113) > (012) were also demonstrated as a result of the rapid formation of Fe^{IV}=O on the surface of the (001) facet.[109] Huang's group indicated that α-Fe_2O_3 nanoparticles stabilized by the carbon matrix showed a high current of 147 mA cm^{-2} at 1.57 V *vs.* RHE, revealing an activity enhancement toward the OER through the construction of the composite.[110] Meanwhile, for another half-reaction of water splitting, *i.e.*, HER, Ali and co-workers prepared α-Fe_2O_3 nanoparticles with controlled size by regulating the pH value of the hydrothermal system.[111] As a result, through setting the pH value as 12, a spherical product with a smaller size was attained,

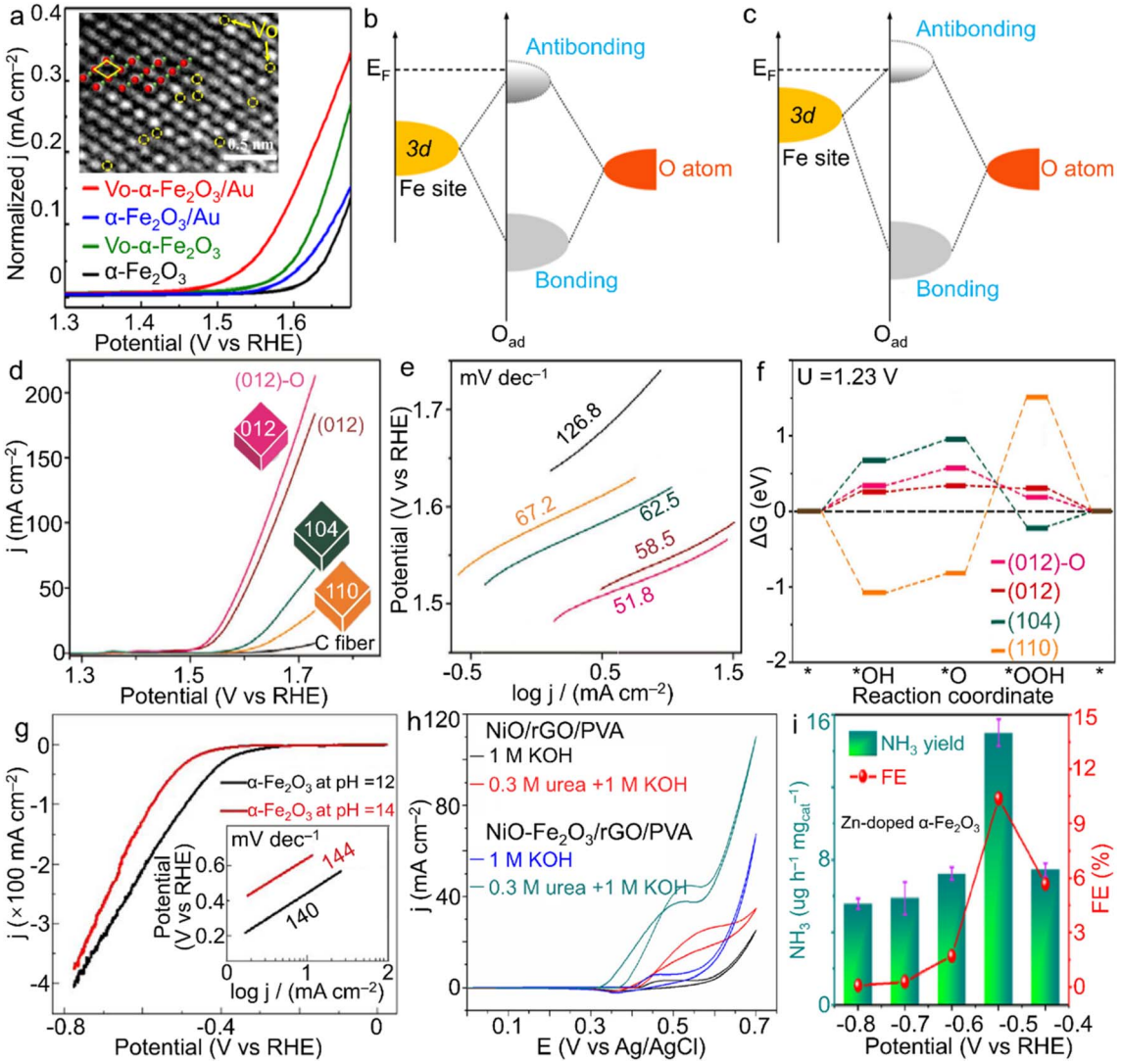

Fig. 5 α-Fe_2O_3 materials for electrocatalysis. (a) LSV plots for vacancy-modified α-Fe_2O_3 samples, and schematic bond formation of O atoms on the α-Fe_2O_3 surface with (b) lower and (c) higher V_O coverages toward the OER. The inset of (a) shows the V_O on the surface of α-Fe_2O_3 crystals, in which green and red spheres stand for oxygen and iron atoms, separately. (a–c) Adapted with permission from ref. 105. Copyright 2022, Elsevier Inc. (d) LSV curves, (e) Tafel slope plots and (f) Gibbs energy change of shaped α-Fe_2O_3 polyhedra for the OER in 1.0 M NaOH electrolyte. Adapted with permission from ref. 108. Copyright 2018, John Wiley & Sons, Inc. (g) HER performance of α-Fe_2O_3 nanoparticles with the tuned size by the pH value of the hydrothermal system. Adapted with permission from ref. 111. Copyright 2018, IOP Publishing. (h) NiO–Fe_2O_3/rGO/PVA for urea oxidation. Adapted with permission from ref. 113. Copyright 2017, Elsevier Inc. (i) Zn-doped α-Fe_2O_3 nanocubes for N_2 fixation. Adapted with permission from ref. 126. Copyright 2021, Elsevier Inc.

gaining more catalytic sites accessible and thus superior activity to the sample prepared under the pH condition of 14 (Fig. 5g). The activity difference verified the possibility of optimizing HER performance by morphology design.

4.1.2. Urea oxidation reaction. Overall water splitting is an effective approach for H_2 generation; however, it needs a high cell voltage due to the sluggish kinetics of the OER. To abate the high energy consumption at the anode, a candidate strategy of replacing the anodic OER with other more feasible electro-oxidation of small molecules was, therefore, proposed. Among them, urea, a non-flammable compound with the formula of CH_4N_2O, widely exists in urine and domestic wastewater. On account of the far lower oxidation potential (~0.37 V *vs.* RHE), anodic urea electrooxidation ($CO(NH_2)_2 + 6OH^- \rightarrow N_2 + 5H_2O + CO_2 + 6e$) is regarded as an excellent half-reaction candidate to the OER for the promotion of rapid H_2 generation.[112,113] Although a favorable driving potential, it possesses much more sluggish reaction kinetics than the typical OER because of the 6-electron-involved process.[114] On the other hand, urea is an energy-enriched compound with an ideal energy density of ~16.9 MJ L^{-1}. Hence, its electrolysis is also evaluated as a potential approach of utilizing urea-rich wastewater to generate electricity *via* direct urea fuel cells.[115] Based on the above considerations, it is challenging to develop high-efficiency catalysts for electrocatalytic urea oxidation. Ni-based nanomaterials, such as NiO and $Ni(OH)_2$, have been extensively studied as energetic

electrocatalysts for urea oxidation.[116–118] To further improve the overall voltage efficiency, additional modifications may be needed. Yoon's group demonstrated that the introduction of α-Fe_2O_3 into the NiO/reduced graphene oxide/poly(vinyl alcohol) (simplified as NiO/rGO/PVA) aerogel could not only significantly reduce the onset oxidation potential (~90 mV) but also enhance the urea oxidation current (Fig. 5h),[119] indicating considerable activity improvements in urea electrooxidation through composition modification.

4.1.3. Nitrogen reduction reaction. Electrocatalytic synthesis of ammonia (NH_3) represents another frontier application of α-Fe_2O_3 materials. NH_3, a significant chemical raw material for agricultural and industrial products such as ammonia solution and fertilizers, is industrially produced in relatively high temperature and pressure environments (400–500 °C and 150–300 bar) using N_2 and H_2 as the feeding gases, *i.e.*, the Haber–Bosch process in which H_2 is primarily produced by the elevated-temperature reaction between carbon-containing compounds and water, and the whole procedure suffers from both enormous energy consumption and CO_2 emission.[120,121] Since the first report using inorganic α-Fe_2O_3-loaded CNTs as a catalyst for electrochemical conversion of N_2 into NH_3 under ambient conditions by Centi's group in 2017, electrocatalytic N_2 reduction reaction (NRR) for the synthesis of NH_3 ($N_2 + 6H_2O \rightarrow 2NH_3 + 6OH^- - 6e$), substantially reducing the reaction temperature with no any greenhouse gas emissions, has attracted great attention.[122] For N_2, the high bond-strength σ and σ* orbital bonds make it rather stable, and a high energy input (~945 kJ mol^{-1}) is required to break the N≡N triple bond directly. In addition, since the theoretical potential of electrochemical N_2 reduction is rather close to that of the HER, a high yield through suppressing the competitive HER is extremely challenging. Meanwhile, the NH_3 product also suffers from the selectivity issue due to the byproduct N_2H_4 ($N_2 + 4H_2O \rightarrow N_2H_4 + 4OH^- - 4e$).[123,124] Considering Fe element as the significant component of both the well-known biological nitrogenase (*i.e.*, Fe-containing proteins) and industrial catalysts for the Haber–Bosch process as well as the advantages of the unoccupied orbitals activating a strong N≡N bond, the oxide form, *i.e.*, α-Fe_2O_3, has gathered a great deal of attention in electrocatalytic NRR for NH_3 generation. For instance, Zhang *et al.* demonstrated oxygen vacancy-rich α-Fe_2O_3 nanocubes with an NH_3 yielding rate and Faradaic efficiency of 32.13 μg h^{-1} mg_{cat}^{-1} and 6.63% at −0.3 V *vs.* RHE in 0.1 M KOH solution, respectively.[125] Moreover, Yu *et al.* introduced low-valence Zn^{2+} into α-Fe_2O_3 nanoparticles for the construction of oxygen vacancies, which contributed to the enhanced N_2 adsorption and was also beneficial to the activation of N_2 molecules. When the doping ratio reached 4.2 at%, a high NH_3 yield rate of 15.1 μg h^{-1} mg_{cat}^{-1} at −0.5 V *vs.* RHE was achieved with a rather considerable faradaic efficiency of 10.4% for NH_3 product in neutral Na_2SO_4 solution (Fig. 5i).[126] Such atom-scale modifications of α-Fe_2O_3 materials make both the high activity and selectivity surpass those of most noble-metal catalysts.

4.1.4. Oxygen reduction reaction. Besides, the oxygen reduction reaction (ORR) acts as a core process for diverse fuel cells (methanol, urea, hydrogen, *etc.*) and aqueous metal–air batteries.[127,128] For the field of energy conversion, the 4-electron-transfer ORR is persistently pursued.[129] Currently, the commercial ORR catalyst for the 4-electron-transfer route is mainly Pt/C material; however, it suffers severely from scarcity and high cost. It is, therefore, imperative to develop much cheaper and more accessible ORR electrocatalysts. Owing to the redox features, α-Fe_2O_3 is a well-studied transition metal oxide; however, its ORR performance is modest and usually inferior to that of Fe_3O_4 spinel because of the deficient electroconductive nature partly. To overcome this shortage, our group constructed α-Fe_2O_3/Fe_3O_4 composites with different compositions by the controlled reduction on α-Fe_2O_3 nanoplates, and unveiled that with the increase of Fe_3O_4, the hydrophilicity decreased gradually, making the active site less accessible (Fig. 6a and b).[130] As a result of composition optimization, the composite which was obtained by setting the reduction as 1 h (denoted as Sample-1h) and consisted of α-Fe_2O_3 (49.6%) and Fe_3O_4 (50.4%) achieved higher activity and selectivity in the 4-electron dominant ORR than the individual α-Fe_2O_3 and Fe_3O_4 as well as other iron oxide composite congeners, as shown in Fig. 6c and d. Moreover, some other electroconductive fundamental phases were also reported to integrate with α-Fe_2O_3 for the construction of high-performance ORR catalysts. For instance, Maiti *et al.* prepared a hybrid of bimetallic oxide α-Fe_2O_3/MoO_3 entrapped N-doped graphene, which presented a superior ORR performance with an electron transfer number of 3.8 and half-wave potential of 0.82 V *vs.* RHE, comparable to a fresh commercial Pt/C electrocatalyst.[131] On the other hand, the two-electron-transfer oxygen reduction process is regarded as a charming strategy for the clean production of H_2O_2 (or H_2O^- in alkaline electrolytes), a value-added chemical that is primarily produced *via* the energy-intensive anthraquinone oxidation process.[132] For common α-Fe_2O_3 materials, the corresponding electron transfer number for the ORR is generally far away from 4, which implies that they may also serve as desirable candidates for promoting the two-electron-involved reduction reaction through careful structure/composition modifications. Gao and co-workers activated the α-Fe_2O_3 single crystals by simultaneous facet and vacancy engineering for intensified H_2O_2 production, as displayed in Fig. 6e and f.[133] It was found that {001} facets were a prerequisite for high selectivity in H_2O_2 generation, while oxygen defects were favorable for the adsorption of O_2 molecules as well as for subsequent protonation into H_2O_2. As a result, a high catalytic activity and selectivity close to 100% toward H_2O_2 generation were realized by oxygen-defective α-Fe_2O_3 nanoplates enclosed by {001} facets (denoted as {001}-Fe_2O_{3-x}), exceeding those of defect-free {001}-Fe_2O_3 as well as {012}-Fe_2O_3 materials with or without oxygen vacancies. Cheng also demonstrated a three-dimensional N-doped α-Fe_2O_3/carbon nanotube composite by calcining the polypyrrole/MIL-101(Fe) precursor.[134] The high selectivity for the H_2O_2 product was uncovered to be altered by the synergistic effect of pyridinic N, pyrrolic N, and α-Fe_2O_3 content, while the activity was determined by the combined merits of graphitic N, oxygen vacancies and CNTs. Since the two-electron-transfer pathway catalyzed by modified α-Fe_2O_3 materials makes it possible to produce H_2O_2 under ambient conditions, future research may

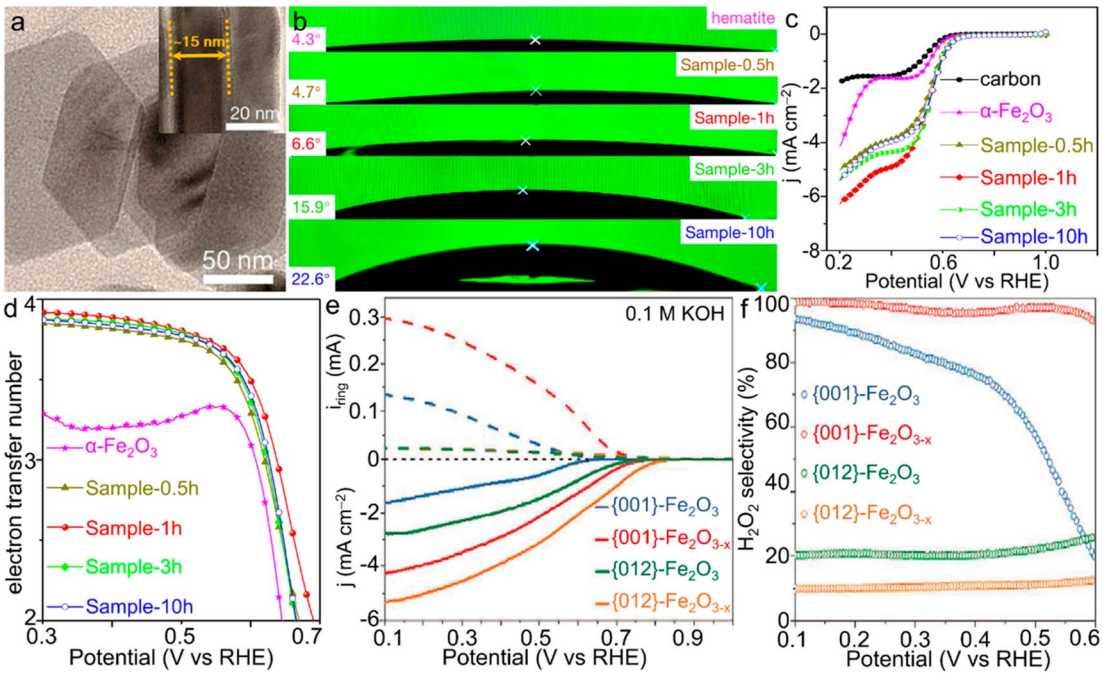

Fig. 6 α-Fe_2O_3 materials for the ORR. (a) TEM image of Sample-1h. (b) Contact angles and (c) LSV curves and (d) electron transfer number of the ORR catalyzed by α-Fe_2O_3/Fe_3O_4 materials with various compositions. (a–d) Adapted with permission from ref. 130. Copyright 2019, American Chemical Society. (e) Rotating ring-disk electrode (RRDE) voltammograms of iron oxides and (f) the corresponding estimated H_2O_2 selectivity of the ORR catalyzed by α-Fe_2O_3 single crystals with simultaneous facet and vacancy engineering. (e and f) Adapted with permission from ref. 133. Copyright 2020, John Wiley & Sons, Inc.

center on the further nanostructure design and composition tuning (*i.e.*, defect engineering), but also the ORR starting from air instead of pure O_2.

4.2. Photocatalysis and photoelectrochemistry

Comparable to electrocatalysis driven by clean electricity resources, photocatalysis and photoelectrochemical reactions involving the capture and utilization of inexhaustible solar energy by semiconductor materials represent another type of significant energy technologies for the production of chemicals and fuels including H_2, N_2H_4, hydrocarbons (C_xH_y) and alcohols, by adopting cheap and readily available raw materials (*i.e.*, H_2O, N_2 and/or CO_2).[135–138] In particular, photochemical conversion of CO_2 into high-value-added fuels and chemicals under natural conditions indicates a promising approach to realizing benign carbon cycling. In the past decades, attempts upon photocatalysis of α-Fe_2O_3 materials were principally made for either the OER or the degradation of organic pollutants such as methyl blue dye. In recent few years, CO_2 reduction photocatalyzed by α-Fe_2O_3 nanostructures was also reported. For a typical α-Fe_2O_3 phase, the small hole diffusion length and the rapid recombination of the photogenerated electron–hole pairs are the dominant factors resulting in an inadequate photocatalytic activity and thus hampering its prevalent applications in photocatalysis.[139–141] In addition, the relatively low conduction band bottom indicates the low-energy photogenerated electrons, which is hardly capable of realizing the reduction reactions of H_2O and CO_2.[142,143]

4.2.1. Photocatalytic CO_2 reduction reaction. The construction of well-designed composites, especially intimate-contact Z-scheme heterostructures consisting of proper fundamental components, is regarded as an effective strategy to overcome these issues maximally. Recently, considering the conduction band of pristine g-C_3N_4 at −1.3 V *vs.* NHE, Wong's group employed it to assemble a hierarchical α-Fe_2O_3/g-C_3N_4 system for photocatalytic CO_2RR.[144] This all-solid-state structure enabled the preferable sites for CO_2 adsorption, and the intimate-contact Z-scheme nanostructure effectively promoted the fast separation of electron–hole pairs, but also increased the reducibility of photogenerated electrons toward a high CO_2-to-CO conversion rate. Similarly, α-Fe_2O_3 with a bandgap and conduction band edge of 1.9 eV and −1.45 V *vs.* RHE was also reported for composting with $SnFe_2O_4$ polyhedra to form a Z-scheme heterostructure, as shown in Fig. 7a.[145] The CO_2RR activity was found to be tuned by the content of α-Fe_2O_3 in the composite. In particular, a premier yield rate of 2.87 μmol g_{cat}^{-1} h^{-1} for CO and 0.64 μmol g_{cat}^{-1} h^{-1} for CH_4, respectively, were delivered when α-Fe_2O_3 possessed a proportion of 12.45 wt%. Besides, other advanced Z-scheme heterostructures based on α-Fe_2O_3, such as α-Fe_2O_3/copper phthalocyanine, α-Fe_2O_3/amine-functionalized reduced graphene oxide/$CsPbBr_3$ and ternary Fe_3N/α-Fe_2O_3/g-C_3N_4,[146–148] have also been proposed for visible-light-driven photocatalytic CO_2RR, showing considerably improved performance compared to single-phase α-Fe_2O_3 materials. It is worth noting that an easily transportable liquid fuel product, methanol (CH_3OH), was photocatalytically

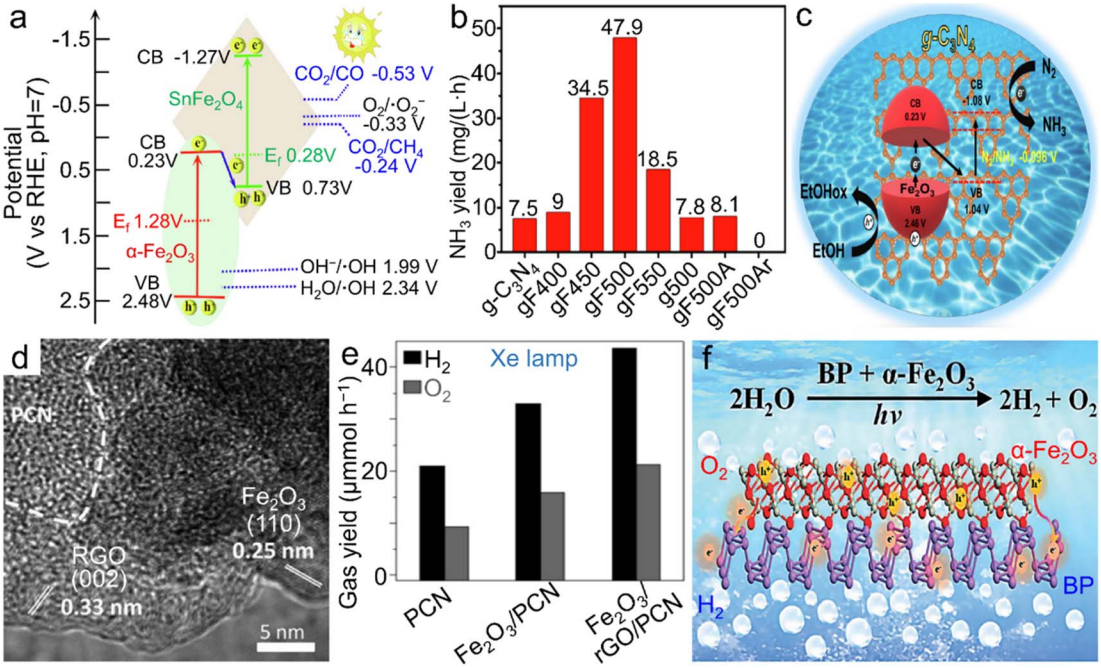

Fig. 7 α-Fe_2O_3 materials for photocatalytic reactions. (a) Band structure of the Z-scheme α-Fe_2O_3/$SnFe_2O_4$ heterostructure for photocatalytic CO_2RR into CO and CH_4. Adapted with permission from ref. 145. Copyright 2020, Elsevier Inc. (b) Photochemical NH_3 yield rate of both pristine g-C_3N_4 and α-Fe_2O_3/g-C_3N_4 calcined at different temperatures and/or atmospheres and (c) the scheme for electronic band structure of α-Fe_2O_3/g-C_3N_4 towards photocatalytic N_2 fixation. (b and c) Adapted with permission from ref. 151. Copyright 2019, John Wiley & Sons, Inc. (d) TEM image and (e) photocatalytic overall water splitting rate of the α-Fe_2O_3/rGO/PCN composite. (d and e) Adapted with permission from ref. 156. Copyright 2019, John Wiley & Sons, Inc. (f) Scheme of the BP/α-Fe_2O_3 photocatalyst for photochemical overall water splitting. Adapted with permission from ref. 157. Copyright 2021, Royal Society of Chemistry.

synthesized in an aqueous CO_2 reduction system in the presence of α-Fe_2O_3/g-C_3N_4 nanoparticles, showing great promise in clean fuel production from inexhaustible CO_2 resources.[149] Incidentally, when it comes to electrocatalytic CO_2RR, Kumar *et al.* demonstrated theoretically that on the (001) surface of an α-Fe_2O_3 slab, CH_3OH would be the preferred product.[150] However, the corresponding practical application has been rarely investigated, and numerous efforts are, therefore, desired on account of the low cost, earth abundance and stability of α-Fe_2O_3 products.

4.2.2. Photocatalytic N_2 reduction reaction. Furthermore, the NRR was also realized by the composites based on α-Fe_2O_3 in photocatalysis. Similar to that in photocatalytic CO_2RR, since the theoretical reduction potential of the N_2-to-NH_3 conversion (*i.e.*, −0.096 V *vs.* NHE) is much more negative than the conduction band minimum, an individual α-Fe_2O_3 phase is hardly capable of carrying out the NRR directly. Namely, the integration of α-Fe_2O_3 with other fundamental semiconductor materials is requisite for the electronic structure tuning and thus the spontaneous photocatalytic conversion under light irradiation. As shown in Fig. 7b and c, Liu *et al.* constructed a Z-scheme α-Fe_2O_3/g-C_3N_4 heterojunction with an α-Fe_2O_3 content less than 1 wt%.[151] In this heterojunction system, calcination temperature was adopted for tuning the light absorbance and the recombination of photogenerated carriers. It was unveiled that even though a rather low α-Fe_2O_3 content existed in such a heterostructure, both an outstanding photocatalytic stability and an NH_3 yield rate of 47.9 mg L^{-1} h^{-1}, ~6 times higher than that of single g-C_3N_4, were gained by the composite prepared at 500 °C (named gF500). Moreover, congeneric photocatalysts, such as α-Fe_2O_3/P-doped TiO_2, were also reported to exhibit considerable activities in visible-light-driven N_2-to-NH_3 conversion,[152] serving as a type of promising photocatalyst for the green synthesis of the NH_3 product.

4.2.3. Photocatalytic overall water splitting. As mentioned above, H_2 may be the ultimate clean fuel resource in the future. Apart from the electrocatalytic approaches, overall water splitting reaction for H_2 generation has also been reported in photocatalysis.[153,154] For a catalyst working for simultaneous production of H_2 and O_2, the conduction band bottom level should be more negative compared to the theoretical H_2O/H_2 reduction potential, while the valence band is required to be located above the standard water oxidation potential. Since single α-Fe_2O_3 materials themselves can only serve as oxygen evolution photocatalysts (OEP), compositing them with other fundamental materials with a matched electronic energy band structure is thus essential to realize the overall water splitting. Alternatively, Z-scheme systems have been verified to show the advantages of not only considerable charge-carrier separation and relatively negative conduction band or positive valence band, but also the function as a bifunctional photocatalyst. The core bottleneck for the construction of Z-scheme heterostructures based on α-Fe_2O_3 materials lies in the development of proper H_2 evolution photocatalysts (HEP) possessing

matched band structures with α-Fe_2O_3 moieties. Polymeric carbon nitride (PCN) is a typical HEP; however, it suffers from intrinsic drawbacks such as a high carrier recombination rate.[155] To further ensure the charge transfer, Pan *et al.* employed rGO as the solid-state electron mediator bridging α-Fe_2O_3 and PCN, as shown in Fig. 7d and e. A markedly improved photocatalytic activity (1.09 and 0.53 mmol g^{-1} h^{-1} for H_2 and O_2, respectively) was delivered by this ternary α-Fe_2O_3/rGO/PCN nanostructure under Xe lamp irradiation.[156] Notably, even under visible light illumination (λ > 400 nm), H_2 and O_2 evolution were concurrently achieved at the rate of 0.22 and 0.12 mmol g^{-1} h^{-1}, respectively, implying a decent bifunctional photocatalyst for overall water splitting under natural sunlight irradiation. Moreover, few-layer black phosphorus (BP) nanosheets with gratifying carrier mobility were also proposed for assembling with α-Fe_2O_3 for the manufacture of a Z-scheme BP/α-Fe_2O_3 photocatalyst, which achieved a stoichiometric ratio of O_2 and H_2 evolution of 0.0586 and 0.0294 mmol g^{-1} h^{-1} under the visible light illumination (λ > 420 nm), separately (Fig. 7f).[157] These frontier case investigations have identified the considerable potential of visible-light-driven overall water splitting by α-Fe_2O_3-based photocatalysts. Future research may be focused on the development of α-Fe_2O_3 materials for the considerable enhancement of overall activity actuated by visible light illumination.

4.2.4. Photoelectrochemistry. In addition to photocatalytic and electrocatalytic strategies for water splitting, the photoelectrochemical (PEC) approach, *i.e.*, solar-driven or solar-assisted electrochemical methods, signifies another attractive strategy toward direct H_2 production. Since the first report of photoelectrochemical water splitting by Fujishima and Honda in 1972, numerous efforts have been dedicated to the development of energetic photocatalysts for PEC reactions.[158] Similar to the conventional photocatalytic applications, typical drawbacks also exist in α-Fe_2O_3 photoanodes, offering a theoretically maximum photocurrent and solar-to-hydrogen efficiency of 12.6 mA cm^{-2} and 16.8% at 1.23 V *vs.* RHE under simulated sunlight illumination, separately.[159] To improve the performance in practical applications, doping strategies were used frequently. For instance, as a result of the co-doping of Ti and Zr, both carrier density and the charge separation were significantly improved, yielding considerable enhancements of PEC performance toward water oxidation.[160] Similarly, a non-metallic S- and/or B-doped α-Fe_2O_3 anode was also demonstrated to deliver a much higher photocurrent than the pristine counterpart.[161,162] On the other hand, another approach of composition modulation, *i.e.*, constructing composites, is also effective for the activity improvement in PEC reaction. Lou's group reported α-Fe_2O_3/TiO_2 microdumbbells with the tips of TiO_2 nanospheres. Compared with the bare α-Fe_2O_3 microrods and TiO_2 nanospheres as well as the physical mixture of these two species, the microdumbbell-like composite showed higher incident photon-to-current conversion efficiency, giving rise to much superior performance in PEC water oxidation.[163] Moreover, Zhang *et al.* combined the composition tuning with structural design, and prepared a TiO_2/α-Fe_2O_3 composite by modifying the surface of α-Fe_2O_3 mesocrystals (a superstructure made of highly ordered nanoparticle (NP) subunits) with a TiO_2 layer, as illustrated in Fig. 8a.[164] Surface reconstruction at the interfaces of the attached subunits was created during the thermal sintering procedure, leading to rich interfacial oxygen defects (denoted as $V_O^{\cdot\cdot}$). Meanwhile, the smaller subunit size (*e.g.*, 5 nm), which was controlled through tuning thermal treatment duration, contributed to the more oxygen defects and the higher carrier density (N_d) as well as the thicker depletion layer. Such modifications created both an exceedingly large N_d value of 4.1 × 10^{21} cm^{-3} and numerous ultranarrow depletion layers with the thickness of ~0.5 nm (Fig. 8b and c), leading to significantly improved hole collection efficiency and thus superior current response in PEC water oxidation. Based on these results, it can be concluded that further downsizing the subunits in α-Fe_2O_3 mesocrystals is worthy of exploration for the further electronic structure modulation and thus the additional performance enhancement.

In addition to water splitting, other PEC reactions were also demonstrated using α-Fe_2O_3 materials. For instance, PEC methanol oxidation was efficiently realized by Pt-loaded α-Fe_2O_3 materials under light illumination (Fig. 8d).[165] A core@shell-like α-Fe_2O_3@Bi_2WO_6 composite was also proposed for the PEC degradation of tetracyclines (TCs), a group of highly stable antibiotics posing a threat to ecological systems, as displayed in Fig. 8e and f.[166] Through controlling the thickness of the α-Fe_2O_3 coating, the optimized performance toward the TC degradation was achieved by the composite with the coating thickness of 15 nm. Owing to the collaboration between light irradiation and the applied electricity, chemical conversions or reactions can proceed more readily compared to those with an individual assistance.

All the abovementioned electrocatalysis, photocatalysis and photoelectrochemistry provide attractive solutions to alleviate energy/environment-related issues such as fossil fuel depletion and CO_2 emissions. In view of the multiple advantages of the α-Fe_2O_3 phase, future efforts to overcome the inherent drawbacks are still encouraged for the continued development as well as industrial use of advanced α-Fe_2O_3 materials.

4.3. Sensors

Chemical sensors based on transition metal compound semiconductors have widespread applications in the fields of agriculture, environmental monitoring, *etc.*[167,168] Among them, α-Fe_2O_3 has been demonstrated to possess multifunctionalities with diverse applications in the gas sensing of acetone and nitrogen oxides, as well as humidity sensors and the aqueous sensing of frontier ions/molecules such as nitrite in the past few years.[169,170] Considerable efforts to enhance the sensing performance have been made through morphology design,[156] constructing composites with other oxides and conductive matrices,[171,172] or heteroatom doping of α-Fe_2O_3 nanostructures.[173]

4.3.1. Sensors for gases. Indoor surroundings are the critical environment associated with our health. In this respect, volatile organic compounds (VOCs) arising from building blocks and/or regional pollution are the most relevant factors,

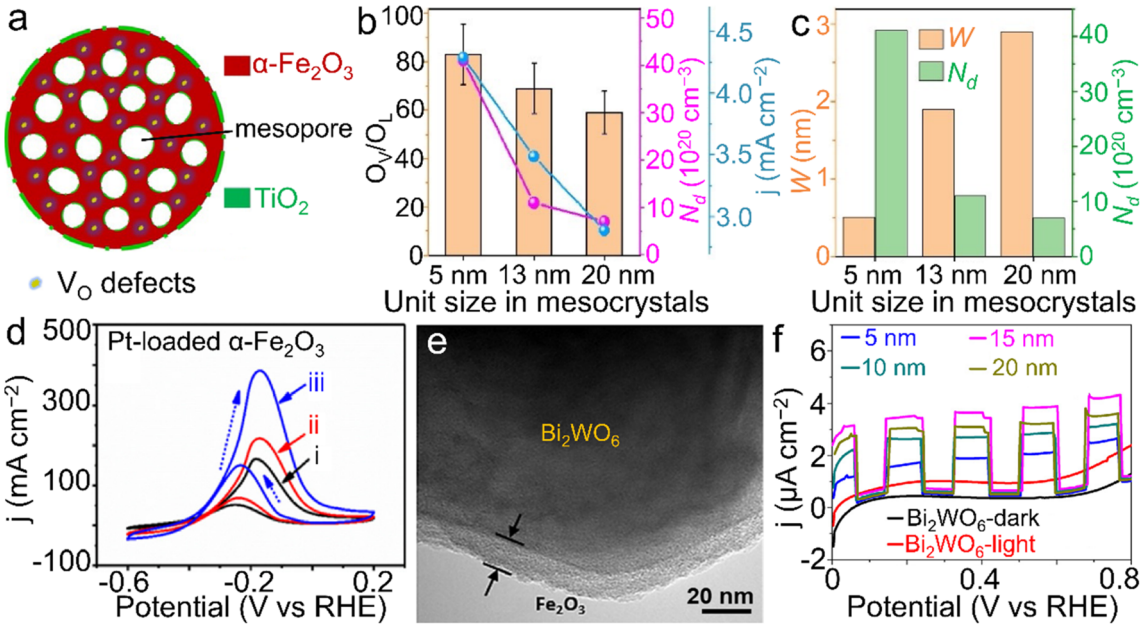

Fig. 8 α-Fe_2O_3 materials for PEC reactions. (a) Structural scheme of TiO_2-modified α-Fe_2O_3 nanospheres with oxygen vacancies toward water oxidation. (b) The relationship between the size of primary subunits, oxygen vacancy ratio (O_V/O_L), carrier density (N_d) and the photocurrent response (j) at 1.23 V *vs.* RHE. (c) The relationship between the depletion width (W), size of primary subunits and N_d of the TiO_2-modified α-Fe_2O_3 product. (a–c) Adapted with permission.[149] Copyright 2020, John Wiley & Sons, Inc. (d) Pt-loaded α-Fe_2O_3 materials for methanol oxidation ((i) in dark; (ii) under visible-light illumination; (iii) simulated solar light illumination). Adapted with permission from ref. 165. Copyright 2019, Elsevier Inc. (e) TEM image of the core@shell-like α-Fe_2O_3@Bi_2WO_6 nanocomposite and (f) α-Fe_2O_3 shell thickness-dependent transient photocurrent responses towards tetracycline (TC) degradation. (e and f) Adapted with permission from ref. 166. Copyright 2019, Elsevier Inc.

and may sustain for several months, leading to adverse effects on our bodies.[174,175] Generally, gas chromatography and/or mass spectrometry are used for the detection of VOCs; however, they need expensive and massive equipment.[176,177] Chemiresistive gas sensors, especially those based on transition metal oxides, have been pursued predominantly because of their superior merits such as cost-effectiveness and simple operation. Among them, p-type semiconductors, such as NiO, have attracted great interest because of the catalytic effect but are beset by a weak response to gaseous analytes when compared with n-type counterparts. Moreover, such a low response may result in poor selectivity toward various gases.[178,179] Combining p-type semiconductors with n-type α-Fe_2O_3 is considered to be an effective approach to modulating the electronic structure and thus the gas sensing properties.[180,181] Suh and co-workers modified the surface of tubular NiO nanoarrays with α-Fe_2O_3 nanoparticles (α-Fe_2O_3 NPs/NiO) and uncovered the increased responses of α-Fe_2O_3 NPs/NiO to gases such as ethanol, toluene (C_7H_8), formaldehyde, *etc.*, in comparison with bare NiO nanoarrays.[182] On the other hand, α-Fe_2O_3 itself is also sensitive to VOCs; nevertheless, it suffers from drawbacks such as dissatisfactory conduction of charge carriers. Kim *et al.* decorated Au nanoparticles on vertical α-Fe_2O_3 nanoarrays (denoted as Au NPs/α-Fe_2O_3) and demonstrated that with this hybrid, most gases could be well-separated, suggesting an exceptional selectivity wherein the theoretical detection limit was calculated to be ~304 ppt for acetone (Fig. 9a–c).[183] Such a detection limit implied the great potential of the Au NPs/α-Fe_2O_3 composite as an acetone sensor. In particular, although humidity induced an inevitable increase of the base resistance, this Au NPs/α-Fe_2O_3 composite showed a substantial response improvement to acetone even under a 50% relative humidity (RH 50%) atmosphere compared to the pure α-Fe_2O_3 sample. Thus far, α-Fe_2O_3 nanomaterials have been studied as humidity sensors in only a few pieces of literature, which indicates a much widespread view of developing cheap sensors based on α-Fe_2O_3 with high selectivity and carrier transport under humid conditions. Also, Zhang *et al.* discovered that an n–n-type α-Fe_2O_3/FeS_2 heterojunction showed a higher response (14.1–100 ppm) and much faster kinetics with a ppb-grade detection limit toward NO_2 gas sensing,[184] as a result of the oxygen spillover effect as well as facilitated electron and mass transfer originating from the interfacial coupling, superior to individual α-Fe_2O_3 and $FeSe_2$ counterparts.

4.3.2. Sensors for liquids. Nitrite, a natural nitrogenous compound, has been proverbially employed as a food additive or preservative.[185,186] Unfortunately, it can react with hemoglobin, causing "blue blood" disease, and/or combine with amines to form carcinogenic nitrosamines.[187,188] Thus, it is imperative to develop sensitive and accurate detection techniques for nitrite in drinking water. Among the various monitoring approaches, electrochemical sensors have aroused worldwide attention on account of the advantages of high sensitivity, fast analysis, *etc.* A multi-component α-Fe_2O_3/protonated carbon nitride/rGO composite (simplified as α-Fe_2O_3/H-C_3N_4/rGO) modified glassy carbon electrode was

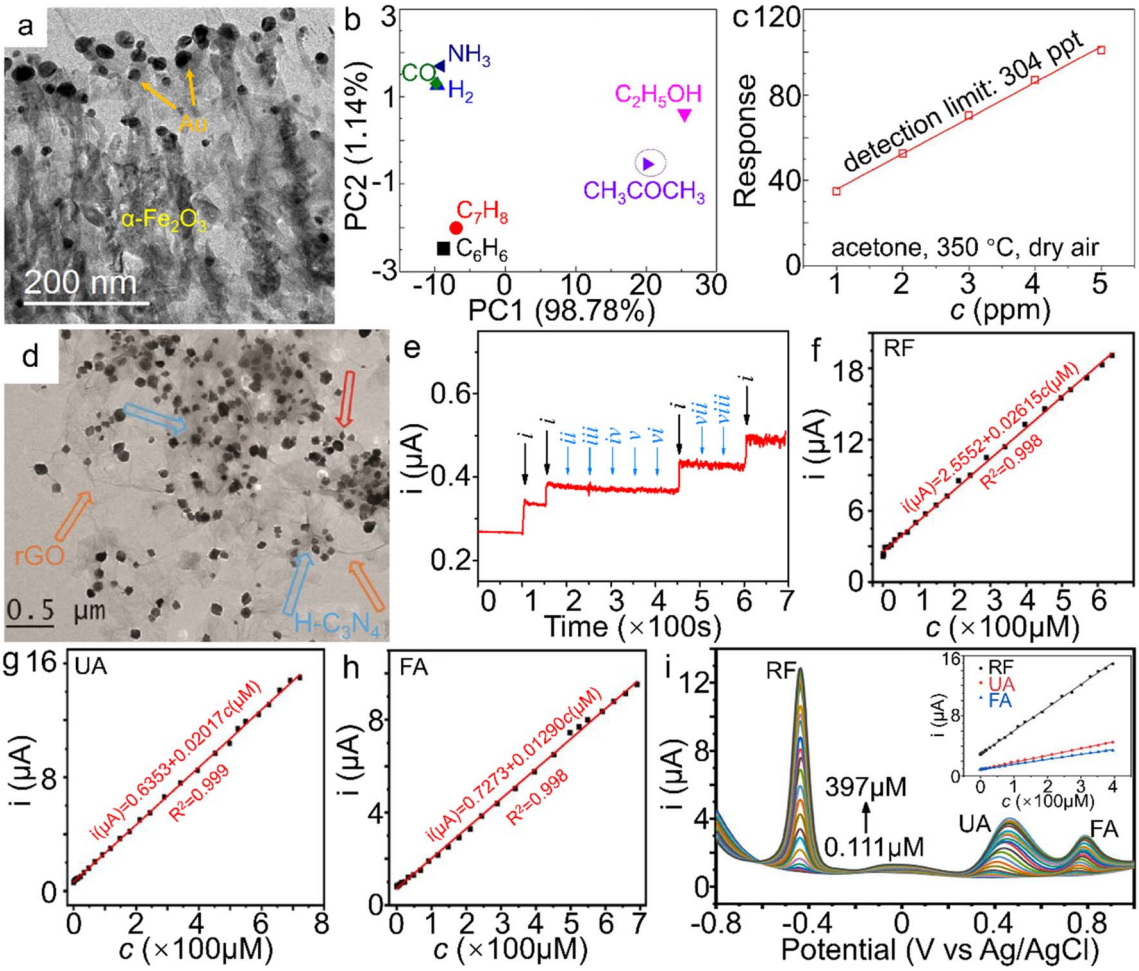

Fig. 9 α-Fe_2O_3 materials for sensor applications. (a) TEM image of Au NPs/α-Fe_2O_3 hybrid, (b) Principle component analysis (PCA) plot on different gases (50 ppm) at 350 °C, (c) the theoretical detection limits (DL) and responses of the α-Fe_2O_3 samples to 50 ppm acetone at 350 °C under a RH 50% atmosphere and dry air. The response value in (c) is defined as R_a/R_g, wherein R_a and R_g stand for the resistance of the sensor in air and target gas, respectively. (a–c) Adapted with permission from ref. 183. Copyright 2018, Elsevier Inc. (d) TEM image of α-Fe_2O_3/H-C_3N_4/rGO. (e) The amperometric response of the α-Fe_2O_3/H-C_3N_4/rGO-modified electrode to $NaNO_2$ in the presence of kinds of interferences in neutral PBS (wherein i, ii, iii, iv, v, vi, vii and viii represent the introduction of $NaNO_2$, NaCl, $MgSO_4$, KNO_3, $ZnSO_4$, $CaCl_2$, glucose and urea additives, respectively). (d and e) Adapted with permission from ref. 189. Copyright 2018, Elsevier Inc. Electrochemical sensing performance of shock wave-treated α-Fe_2O_3 nanoparticles on (f) RF, (g) UA, (h) FA and (i) RF, UA and FA simultaneously. (f–i) Adapted with permission from ref. 195. Copyright 2021, Elsevier Inc.

proposed for the detection of $NaNO_2$, as shown in Fig. 9d,[189] which showed a high sensing accuracy with the detection limit as low as 0.407 μM, meeting the requirements established by the World Health Organization (<3.0 mg L^{-1}).[190,191] Fig. 9e displays the amperometric response of the modified electrode to kinds of interferences, which explicitly confirms the high selectivity of the ternary α-Fe_2O_3/H-C_3N_4/rGO composite toward NO_2^-. On the other hand, vitamins are indispensable micronutrients for body tissues. Among them, the vitamin B group possesses important functions in maintaining normal physiology. Riboflavin ($C_{17}H_{20}N_4O_6$, RF), *i.e.*, hydrosoluble vitamin B2, is essential for muscle strength, motor function, hearing, vision, and tissue respiration.[192] In other words, it can exclusively be acquired from food. Folic acid ($C_{19}H_{19}N_7O_6$, FA), known as vitamin B9, is required for cell growth, amino acid metabolism, the formation of blood cells, and regular cell division. The concentration of FA is tightly associated with a variety of diseases including hypercholesterolemia and hypertension, and overdose is also not allowed.[193] Furthermore, uric acid ($C_5H_4N_4O_3$, UA), the primary metabolite of purines, mainly exists in biological fluids such as urine and can act as an indicator reflecting diseases such as gout and hyperuricemia.[194] It is, therefore, of great significance to detect UA concentration for pathological diagnosis. Since these three organic compounds are compositionally similar and may present in biological fluids simultaneously, it is rather difficult to detect them precisely. Recently, Meenakshi adopted shock pulses for the rapid preparation of α-Fe_2O_3 nanoparticles with a smaller size of ~20 nm, while that for the pristine counterparts was in the range of 25–33 nm.[195] Both the high selectivity and concurrent determination ability toward RF, UA, and FA in 0.1 M PBS (pH = 7.4) were achieved by the nanoparticle-

modified glassy carbon electrode, as displayed in Fig. 9f–i. For selective detection, the electrode created wide dynamic ranges of 0.11 to 624 μM for RF, 0.11 to 722 μM for UA, and 0.11 to 691 μM for FA with the corresponding minimum limits of 26, 18, and 25 nM, separately. More importantly, the α-Fe_2O_3 sensor for determining the organics showed satisfactory stability. This study pioneered a promising strategy with tremendous potential for the detection of compositionally similar organic analogs.

4.4. Biological medicine

4.4.1. Magnetic resonance imaging. On account of their biocompatibility and low toxicity, α-Fe_2O_3 materials are also cherished in biological medicine. In the past, those with hollow interiors were extensively studied in drug delivery and antibacterial applications.[196–199] Recently, they have also been reported in several emerging fields of biomedicine. Magnetic resonance imaging (MRI) is an efficient tool for the detection of pathological tissues. While for the T_1-weighted counterpart, its signal is directly determined by longitudinal-spin lattice relaxation time that can be shortened through the intimate interactions between water protons and the surrounding paramagnetic metal ions. These ions generally possess abundant unpaired electrons of high-spin states, *e.g.*, Mn^{2+}, Fe^{3+} and Gd^{3+}.[200–202] Clinically, a Gd^{3+}-containing chelate named gadolinium diethylenetriamine penta-acetic acid (Gd-DTPA) is widely used as the contrast agent.[203] On the other hand, in frontier research, other Gd-based compounds, such as oxides and phosphates,[204–207] also awoke great interest. Indeed, these materials have achieved considerable contrast effects but unfortunately suffer from high cost and inherent physiological toxicity. In particular, they are not suitable for all patients, especially those plagued by renal insufficiency.[208] Developing other relatively safe contrast agents for T_1-weighted MRI is, therefore, greatly urgent. Recently, our team first proposed Gd-doped α-Fe_2O_3 nanoparticles with the dopant concentration of 5.7 at%, as shown in Fig. 10.[209] Through the atom-scale introduction of Gd^{3+} ions with half-occupied 4f electronic configuration, both the magnetic structure and total magnetic moment of the pristine α-Fe_2O_3 material were substantially changed owing to the strong synergistic effect of O-s and Gd-p electronic orbitals along with the enlarged long-range dipolar interactions from the spindle-like nanostructure. When the doping ratio reached 5.7 at%, numerous unpaired electrons and higher-spin states were created, promoting the ambient protons to yield much shortened longitudinal relaxation effects. As a result, the doped α-Fe_2O_3 nanoparticles showed a clear contrast effect for *in vitro* T_1-weighted MRI compared to the undoped counterpart. Moreover, even in the tumor tissue of a nude mouse, an efficient contrast was achieved by the Gd-doped α-Fe_2O_3 product. Although such a contrast effect was inferior to those of Gd-containing compounds, this innovation pioneered a novel strategy for the development of low-toxicity T_1-weighted MRI contrast agents. Tadic and co-workers further disclosed that downsizing to ~30 nm, α-Fe_2O_3 nanocrystals presented an improved T_2 relaxation.[34] On account of the contrast effect of the Gd-doped α-Fe_2O_3 sample, it may further composite with T_2-weighted contrast materials (*i.e.*, superparamagnetic Fe_3O_4 and γ-Fe_2O_3) for T_1- and T_2-weighted dual mode MRI. Also, surface modifications of inorganic nanoparticles with biocompatible organics, such as D-glucuronic acid and derivatives of polyethylene glycol,[210–212] need to be carried out for better *in vivo* contrast effects.

4.4.2. Hemostasis. In traditional Chinese medicine, hematitum consisting of α-Fe_2O_3 and silica was orally admitted and applied externally for the treatment of hemostasis. On the other hand, tracing back to 2014, commercial α-Fe_2O_3 nanoparticles

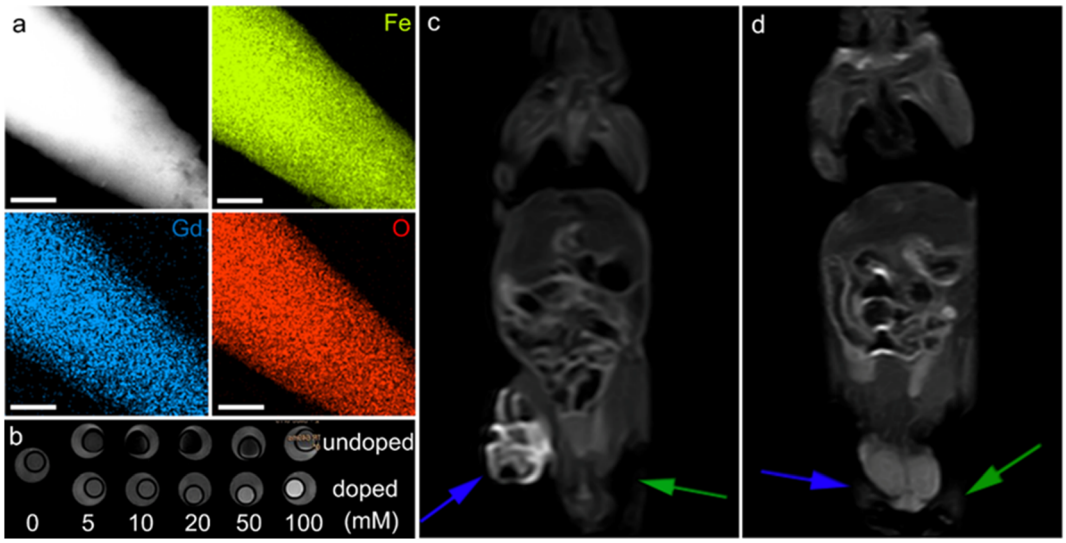

Fig. 10 α-Fe_2O_3 materials for MRI. (a) Elemental mapping of Gd-doped α-Fe_2O_3 nanoparticles, the scale bar is 200 nm. (b) *In vitro* T_1-weighted MRI contrast of undoped and doped α-Fe_2O_3 materials. *In vivo* contrast effects of (c) the doped and (d) undoped α-Fe_2O_3 samples. The blue and green arrows in (c and d) stand for the tumors injected with α-Fe_2O_3 dispersions and the blank experiments, respectively. (a–d) Adapted with permission from ref. 209. Copyright 2017, John Wiley & Sons, Inc.

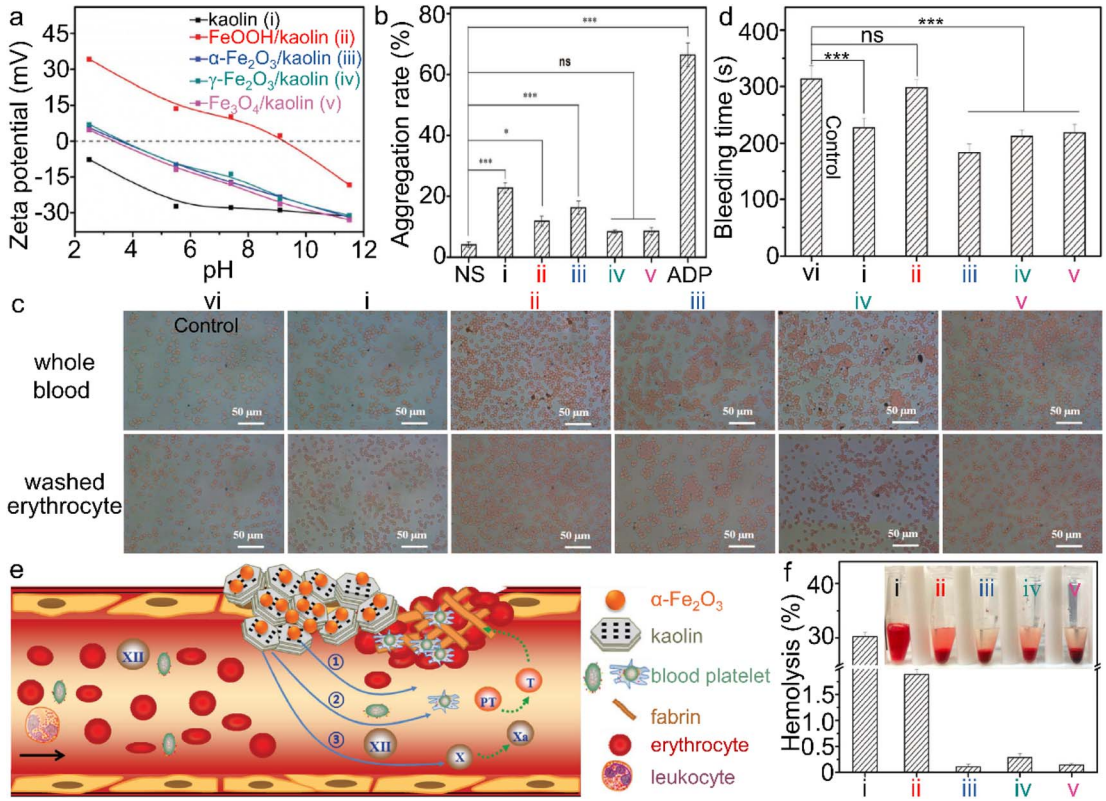

Fig. 11 α-Fe_2O_3/kaolin composite for hemolysis. (a) Zeta potential of kaolin and different iron (hydr)oxide/kaolin samples. (b) Platelet aggregation, and (d) bleeding time of the wounds, treated by different iron (hydr)oxide samples, wherein ns and ADP stand for normal saline and adenosine diphosphate, respectively. (c) Interaction between iron (hydr)oxide/kaolin samples and red blood cells. (e) Scheme of the synergism of the α-Fe_2O_3/kaolin composite for hemostasis and (f) hemolysis test. Adapted with permission from ref. 214. Copyright 2018, John Wiley & Sons, Inc.

were applied to tissue repairs by Meddahi-Pellé *et al.*, and were evidenced to induce rapid wound closure,[213] indicating the great potential of α-Fe_2O_3 in nanomedicine. However, the hemostasis properties of α-Fe_2O_3 have been rarely investigated in detail until Yang's group proposed an α-Fe_2O_3/kaolin composite (wherein kaolin was an aluminosilicate clay with a chemical formula of $Al_2Si_2O_5(OH)_4$) in 2018.[214] This aluminosilicate possessed a negatively charged surface and the negative zeta potential was even larger under the higher pH conditions. After the combination with various iron oxides, more positive zeta potentials were yielded; however, they were still negative at ~7.4 (*i.e.*, the pH value of human blood), while the FeOOH/kaolin hybrid had the highest isoelectric point (~9.2), as depicted in Fig. 11a. As a result of the surface charge properties, kaolin exhibited the largest water adsorption capacity of 123.9%, while those for α-Fe_2O_3/kaolin, γ-Fe_2O_3/kaolin and Fe_3O_4/kaolin were 106.6%, 95.3%, and 108.1%, separately, while FeOOH/kaolin possessed the lowest value of 77.9%. In addition, the surface charge might also influence the platelet aggregation rate; that is, the maximum of 22.7 ± 1.7% was achieved by kaolin, followed by 16.2 ± 2.2% and 11.8 ± 1.6% for α-Fe_2O_3/kaolin and FeOOH/kaolin, respectively, while for the interactions between iron (hydr)oxide/kaolin samples and red blood cells, as depicted in Fig. 11b and c, the most pronounced effect on promoting the aggregation of red blood cells was observed for α-Fe_2O_3/kaolin, implying a rapid formation of blood clots due to the addition of α-Fe_2O_3 when compared with the sole kaolin. The hemostatic activity was directly associated with liquid adsorption and the interactions with blood cells.[215] In addition, the negatively charged surface of α-Fe_2O_3/kaolin induced the conversion of FXII into FXIIA, accelerating the generation of thrombin and thus the formation of fibrin, beneficial for efficient hemorrhage control. With the combined merits of α-Fe_2O_3 and kaolin, rapid hemostasis of ~183 s was achieved, as shown in Fig. 11d and e. Furthermore, the α-Fe_2O_3/kaolin composite showed a negligible hemolysis degree (*i.e.*, satisfactory biocompatibility), revealing that it was a safe hemostatic agent (Fig. 11f). Considering the advantages of both low toxicity and easy access, further performance improvements as well as other promising applications associated with biomedicine are desired for α-Fe_2O_3 materials.

5. Conclusions

In summary, this work provided an overview of the recent progress in the fabrication of advanced α-Fe_2O_3 materials with elaborate nanostructures/compositions and their applications in some newly emerging fields such as electrocatalysis, some specific photo(electro)chemical reactions, sensors and biological medicine. In particular, a detailed focus on the relationship

between nanostructure/composition-induced electronic structure modulation and the practical capabilities in various applications was presented. The nanostructure engineering as well as the broad choice of both doping heteroatoms and the compositing fundamental components implies that a wide variety of α-Fe_2O_3 materials can be synthesized with optimized physicochemical properties. Although significant breakthroughs have been made in these emerging fields, limited by the primitive physicochemical features of the pure α-Fe_2O_3 phase, further improvements are still desired but it is challenging.

Based on the current perspectives, it is worth carrying out more in-depth explorations into fabrication strategies, physicochemical properties and practical applications in future research. Herein we propose several research orientations or opportunities for the prospective developments of functional materials based on α-Fe_2O_3.

(i) It is anticipated to develop some modified and/or novel approaches for the preparation of designed α-Fe_2O_3 materials, especially those with great potential for industrial use. It is well known that the nanostructure and composition, which are substantially determined by the synthetic procedures, are the two main factors influencing the electronic structure and thus the physicochemical properties as well as the performance. It is of great interest to engineer both lattices and defects since the interior strain force and defects can considerably modulate the electronic structure of α-Fe_2O_3 and thus endow it with relatively high internal energy and/or activities, *i.e.*, modify the relatively inert redox features.

(ii) Constructing α-Fe_2O_3-based inorganic-organic hybrids may offer a promising approach for the extension of functional materials. The reported composites of α-Fe_2O_3 are almost made of all-inorganic-state forms. Compared to inorganic materials, the organic components including monomers and polymers contain infinite variants of species available and the chemical bonds may be more flexible for electronic structure modulation, indicating rich physicochemical properties for various kinds of hybrid functional materials.

(iii) The continued development and utilization of various kinds of advanced characterization techniques, especially *in situ* monitoring counterparts such as Raman measurements for the identification of intermediates in aqueous catalytic reactions, are required for deep insight into the interaction mechanisms of α-Fe_2O_3 materials in various applications.

(iv) For α-Fe_2O_3 materials applicable for *in vivo* biological medicine, it is essential to further downsize the nanoparticles (*e.g.*, less than 100 nm) but also improve the dispersity through surface ligand modifications. The use of particles with too large size and/or inferior dispersity may result in localized embolization issues.

(v) High-throughput sieving of high-performance α-Fe_2O_3 materials through machine learning is encouraged. Currently, nearly all the studies have utilized manual trial-and-error routes to determine which fundamental material is more applicable to a specific application system. Through robotics-based computational screening, the trial-and-error procedure can be efficiently accelerated.

(vi) α-Fe_2O_3 materials are also highly expected in other frontier fields through rational electronic structure modulation, in particular multidisciplinary applications, such as *in vivo* dual-mode MRI contrast agents, targeted therapy, electrocatalytic CO_2 reduction, *etc.*

Undoubtedly, the recent progress indicates a bright future for α-Fe_2O_3 materials in emerging applications. As a result of the careful combination of nanostructure design and a diverse choice of either doping heteroatoms or coupling with fundamental phase species, electronic structure tuning associated with marvelous properties will be realized. It is believed that α-Fe_2O_3 materials with a specific nanostructure/composition are capable of delivering incredible performance appropriate for the applications including but not limited to the above aspects. Furthermore, this review will also offer a deep insight into the design of other transition metal-based compounds as well as their composites as functional materials for plenty of cutting-edge fields.

Author contributions

H. W. and R. M. conceived the idea. X. L., Y. Z. and R. M supervised the project. The manuscript was written through the contributions of all authors. All authors have given approval to the final version of the manuscript.

Conflicts of interest

There are no conflicts to declare.

Acknowledgements

This work was financially supported by the National Natural Science Foundation of China (U20A20123, 51874357), the Hunan Provincial Natural Science Foundation of China (2019JJ10006), and Henan Provincial Key Technology R&D Program (222102240089, 212102210597). H. W. is thankful for the support from the Youth Talent Program of Zhengzhou University.

Notes and references

1 Z. Zheng, Y. Lu and Q. Li, *Adv. Mater.*, 2020, **32**, 1905318.
2 K. Bernot, C. Daiguebonne, G. Calvez, Y. Suffren and O. Guillou, *Acc. Chem. Res.*, 2021, **54**, 427.
3 L. Wang, D. Chen, K. Jiang and G. Shen, *Chem. Soc. Rev.*, 2017, **46**, 6764.
4 Y. Li, X. Wei, L. Chen and J. Shi, *Angew. Chem., Int. Ed.*, 2021, **60**, 19550.
5 J. Ćwik, Y. Koshkid'ko, N. A. de Oliveira, K. Nenkov, A. Hackemer, E. Dilmieva, N. Kolchugina, S. Nikitin and K. Rogacki, *Acta Mater.*, 2017, **133**, 230.
6 Y. Lin, H. Wan, D. Wu, G. Chen, N. Zhang, X. Liu, J. Li, Y. Cao, G. Qiu and R. Ma, *J. Am. Chem. Soc.*, 2020, **142**, 7317.
7 F. Chen, C. Yang, X. Liu, N. Zhang, P. Rong, S. Liang and R. Ma, *ACS Sustainable Chem. Eng.*, 2018, **6**, 10463.

8 C. Liao, B. Yang, N. Zhang, M. Liu, G. Chen, X. Jiang, G. Chen, J. Yang, X. Liu, T.-S. Chan, Y.-J. Lu, R. Ma and W. Zhou, *Adv. Funct. Mater.*, 2019, **29**, 1904020.
9 Y. Yuan, J. Wang, S. Adimi, H. Shen, T. Thomas, R. Ma, J. P. Attfield and M. Yang, *Nat. Mater.*, 2020, **19**, 282.
10 C. Chen, W. Xue, S. Li, Z. Zhang, X. Li, X. Wang, Y. Liu, J. Sui, X. Liu and F. Cao, *Proc. Natl. Acad. Sci. U. S. A.*, 2019, **116**, 2831.
11 L.-C. Hsu, H.-C. Yu, T.-H. Chang and Y.-Y. Li, *ACS Appl. Mater. Interfaces*, 2011, **3**, 3084.
12 Z. Zhang, Md. F. Hossain and T. Takahashi, *Appl. Catal., B*, 2010, **95**, 423.
13 Y. Jian, T. Yu, Z. Jiang, Y. Yu, M. Douthwaite, J. Liu, R. Albilali and C. He, *ACS Appl. Mater. Interfaces*, 2019, **11**, 11369.
14 M. Ates, I. C. C. Cimen, I. Unal, B. Kutlu, B. Ertit Tastan, D. Danabas, O. Aksu and Z. Arslan, *Environ. Toxicol.*, 2020, **35**, 385.
15 G. Chen, L. Yan, H. Luo and S. Guo, *Adv. Mater.*, 2016, **28**, 7580.
16 W. Zhou, C. Cheng, J. Liu, Y. Y. Tay, J. Jiang, X. Jia, J. Zhang, H. Gong, H. H. Hng and T. Yu, *Adv. Funct. Mater.*, 2011, **21**, 2439.
17 Y. Zhu, S. Cheng, W. Zhou, J. Jia, L. Yang, M. Yao, M. Wang, J. Zhou, P. Wu and M. Liu, *ACS Sustainable Chem. Eng.*, 2017, **5**, 5067.
18 L. Guo, F. Chen, X. Fan, W. Cai and J. Zhang, *Appl. Catal., B*, 2010, **96**, 162.
19 G. Qiu, H. Huang, H. Genuino, N. Opembe, L. Stafford, S. Dharmarathna and S. L. Suib, *J. Phys. Chem. C*, 2011, **115**, 19626.
20 F. Meng, J. Li, S. K. Cushing, J. Bright, M. Zhi, J. D. Rowley, Z. Hong, A. Manivannan, A. D. Bristow and N. Wu, *ACS Catal.*, 2013, **3**, 746.
21 J. Huang, X. Liu, G. Chen, N. Zhang, R. Ma and G. Qiu, *Solid State Sci.*, 2018, **82**, 24.
22 F. Bødker, M. F. Hansen, C. B. Koch, K. Lefmann and S. Mørup, *Phys. Rev. B: Condens. Matter Mater. Phys.*, 2000, **61**, 6826.
23 E. D. Negri, O. M. Alfano and M. G. Chiovetta, *Ind. Eng. Chem. Res.*, 1991, **30**, 474.
24 H.-J. Freund, G. Meijer, M. Scheffler, R. Schlögl and M. Wolf, *Angew. Chem., Int. Ed.*, 2011, **50**, 10064.
25 X. Lu, Y. Zeng, M. Yu, T. Zhai, C. Liang, S. Xie, M.-S. Balogun and Y. Tong, *Adv. Mater.*, 2014, **26**, 3148.
26 B. Klahr, S. Gimenez, F. Fabregat-Santiago, T. Hamann and J. Bisquert, *J. Am. Chem. Soc.*, 2012, **134**, 4294.
27 F. Ye, Y. Hu, Y. Zhao, D. Zhu, Y. Wang, M. Pu and S. S. Mao, *J. Mater. Chem. A*, 2016, **4**, 14687.
28 G. Chen, R. Rodriguez, L. Fei, Y. Xu, S. Deng, S. Smirnov and H. Luo, *J. Power Sources*, 2014, **259**, 227.
29 S. Chen, S. Perathoner, C. Ampelli, H. Wei, S. Abate, B. Zhang and G. Centi, *J. Energy Chem.*, 2020, **49**, 22.
30 C. T. Moi, S. Bhowmick, T. K. Sahu and M. Qureshi, *Electrochim. Acta*, 2021, **370**, 137726.
31 L. Long, G. Lv, Q. Han, X. Wu, Y. Qian, D. Wang, Y. Zhou and Z. Zou, *J. Phys. Chem. C*, 2021, **125**, 23142.
32 Y. Piekner, D. S. Ellis, D. A. Grave, A. Tsyganok and A. Rothschild, *Energy Environ. Sci.*, 2021, **14**, 4584.
33 M. Ma, L. Peng, J. Li, Y. Zhang, Z. Wang, J. Bi, D. Gao and J. Wu, *Sens. Actuators, B*, 2021, **339**, 129907.
34 M. Tadic, L. Kopanja, M. Panjan, J. Lazovic, B. V. Tadic, B. Stanojevic and L. Motte, *Mater. Res. Bull.*, 2021, **133**, 111055.
35 Y. Xue and Y. Wang, *Nanoscale*, 2020, **12**, 10912.
36 X. Huang, X. Hou, X. Zhang, K. M. Rosso and L. Zhang, *Environ. Sci.: Nano*, 2018, **5**, 1790.
37 J. Li, H. Chen, C. A. Triana and G. R. Patzke, *Angew. Chem., Int. Ed.*, 2021, **60**, 18380.
38 Z. Najaf, D. L. T. Nguyen, S. Y. Chae, O.-S. Joo, A. U. H. A. Shah, D.-V. N. Vo, V.-H. Nguyen, Q. V. Le and G. Rahman, *Int. J. Hydrogen Energy*, 2021, **46**, 23334.
39 C. Li, Z. Luo, T. Wang and J. Gong, *Adv. Mater.*, 2018, **30**, 1707502.
40 M. Catti, G. Valerio and R. Dovesi, *Phys. Rev. B: Condens. Matter Mater. Phys.*, 1995, **51**, 7441.
41 S. Capone, M. Benkovicova, A. Forleo, M. Jergel, M. G. Manera, P. Siffalovic, A. Taurino, E. Majkova, P. Siciliano, I. Vavra, S. Luby and R. Rella, *Sens. Actuators, B*, 2017, **243**, 895.
42 D. Mao, J. Yao, X. Lai, M. Yang, J. Du and D. Wang, *Small*, 2011, **7**, 578.
43 C. A. Lanzl, J. Baltrusaitis and D. M. Cwiertny, *Langmuir*, 2012, **28**, 15797.
44 A. A. Zatsiupa, L. A. Bashkirov, I. O. Troyanchuk, G. S. Petrov, A. I. Galyas, L. S. Lobanovsky and S. V. Truhanov, *J. Solid State Chem.*, 2014, **212**, 147.
45 R. N. Bhowmik and A. Saravanan, *J. Appl. Phys.*, 2010, **107**, 053916.
46 D. Kubániová, L. Kubíčková, T. Kmječ, K. Závěta, D. Nižňanský, P. Brázda, M. Klementová and J. Kohout, *J. Magn. Magn. Mater.*, 2019, **475**, 611.
47 I. V. Golosovsky, I. Mirebeau, F. Fauth, D. A. Kurdyukov and Yu. A. Kumzerov, *Solid State Commun.*, 2007, **141**, 178.
48 J. Velev, A. Bandyopadhyay, W. H. Butler and S. Sarker, *Phys. Rev. B: Condens. Matter Mater. Phys.*, 2005, **71**, 205208.
49 H. B. Na and T. Hyeon, *J. Mater. Chem.*, 2009, **19**, 6267.
50 K. An, M. Park, J. H. Yu, H. B. Na, N. Lee, J. Park, S. H. Choi, I. C. Song, W. K. Moon and T. Hyeon, *Eur. J. Inorg. Chem.*, 2012, **12**, 2148.
51 K. Y. Ju, J. W. Lee, G. H. Im, S. Lee, J. Pyo, S. B. Park, J. H. Lee and J. K. Lee, *Biomacromolecules*, 2013, **14**, 3491.
52 Q. Zhu, C. Yu and X. Zhang, *J. Energy Chem.*, 2019, **35**, 30.
53 J. Li, F. Meng, S. Suri, W. Ding, F. Huang and N. Wu, *Chem. Commun.*, 2012, **48**, 8213.
54 G. Shen, L. Pan, R. Zhang, S. Sun, F. Hou, X. Zhang and J. Zou, *Adv. Mater.*, 2020, **32**, 1905988.
55 Y. Zhao, C. Deng, D. Tang, L. Ding, Y. Zhang, H. Sheng, H. Ji, W. Song, W. Ma, C. Chen and J. Zhao, *Nat. Catal.*, 2021, **4**, 684.
56 C. Li, Z. Luo, T. Wang and J. Gong, *Adv. Mater.*, 2018, **30**, 1707502.
57 H. Kang, D. Lee, K.-M. Lee, H.-H. Kim, H. Lee, M. Sik Kim and C. Lee, *Chem. Eng. J.*, 2021, **426**, 130743.

58 K. Kamiya, A. Kuwabara, T. Harada and S. Nakanishi, *ChemPhysChem*, 2019, **20**, 648.
59 N. Thüns, B. M. Krooss, Q. Zhang and H. Stanjek, *Int. J. Hydrogen Energy*, 2019, **44**, 27615.
60 Y. Wang, J. Han, X. Gu, S. Dimitrijev, Y. Hou and S. Zhang, *J. Mater. Chem. A*, 2017, **5**, 18737.
61 P. Y. Tang, L. J. Han, A. Genç, Y. M. He, X. Zhang, L. Zhang, J. R. Galán-Mascarós, J. R. Morante and J. Arbiol, *Nano Energy*, 2016, **22**, 189.
62 H. Liu, K. Tian, J. Ning, Y. Zhong, Z. Zhang and Y. Hu, *ACS Catal.*, 2019, **9**, 1211.
63 M. Su, C. He and K. Shih, *Ceram. Int.*, 2016, **42**, 14793.
64 Z. Wu, Z. Li, H. Li, M. Sun, S. Han, C. Cai, W. Shen and Y. Fu, *ACS Appl. Mater. Interfaces*, 2019, **11**, 12761.
65 M. Mohammadikish, *Ceram. Int.*, 2014, **40**, 1351.
66 T. P. Almeida, M. W. Fay, Y. Zhu and P. D. Brown, *Nanoscale*, 2010, **2**, 2390.
67 T. Chen, W. Jiang, X. Sun, W. Ning, Y. Liu, G. Xu and G. Han, *ChemistrySelect*, 2020, **5**, 430.
68 S. B. Wang, Y. L. Min and S. H. Yu, *J. Phys. Chem. C*, 2007, **111**, 3551.
69 S. Muniyappan and P. Murugakoothan, *Mater. Lett.*, 2018, **220**, 277.
70 G. Gao, X. Liu, R. Shi, K. Zhou, Y. Shi, R. Ma, E. Takayama-Muromachi and G. Qiu, *Cryst. Growth Des.*, 2010, **10**, 2888.
71 P. Andreakou, M. Brossard, C. Li, M. Bernechea, G. Konstantatos and P. G. Lagoudakis, *J. Phys. Chem. C*, 2013, **117**, 1887.
72 X. C. Jiang, A. B. Yu, W. R. Yang, Y. Ding, C. X. Xu and S. Lam, *J. Nanopart. Res.*, 2010, **12**, 877.
73 L. Li, Y. Chu, Y. Liu and L. Dong, *J. Phys. Chem. C*, 2007, **111**, 2123.
74 D. M. G. T. Nathan and S. J. M. Boby, *J. Alloys Compd.*, 2017, **700**, 67.
75 Z. Zhao, X. Wang, J. Si, C. Yue, C. Xia and F. Li, *Green Chem.*, 2018, **20**, 832.
76 C. Zhang, F. Zheng, Z. Zhang, D. Xiang, C. Cheng, Z. Zhuang, P. Li, X. Li and W. Chen, *J. Mater. Chem. A*, 2019, **7**, 9059.
77 X. Huang, Y. Chen, E. Walter, M. Zong, Y. Wang, X. Zhang, O. Qafoku, Z. Wang and K. M. Rosso, *Environ. Sci. Technol.*, 2019, **53**, 10197.
78 S. Wu, Y. He, C. Wang, C. Zhu, J. Shi, Z. Chen, Y. Wan, F. Hao, W. Xiong, P. Liu and H. Luo, *ACS Appl. Mater. Interfaces*, 2020, **12**, 26733.
79 L. Sun, W. Zhan, Y.-A. Li, F. Wang, X. Zhang and X. Han, *Inorg. Chem. Front.*, 2018, **5**, 2332.
80 P. Li, J. Ji, X. Deng, A. Li, J. Hu, G. Li and W. Zhang, *CrystEngComm*, 2015, **17**, 7283.
81 A. K. Patra, S. K. Kundu, A. Bhaumik and D. Kim, *Nanoscale*, 2016, **8**, 365.
82 H. Wan, T. Liu, X. Liu, J. Pan, N. Zhang, R. Ma, S. Liang, H. Wang and G. Qiu, *RSC Adv.*, 2016, **6**, 66879.
83 D. Ding, Y. Huang, C. Zhou, Z. Liu, J. Ren, R. Zhang, J. Wang, Y. Zhang, Z. Lei, Z. Zhang and C. Zhi, *ACS Appl. Mater. Interfaces*, 2016, **8**, 142.
84 J. Xie, W. Liu, J. Xin, F. Lei, L. Gao, H. Qu, X. Zhang and Y. Xie, *ChemSusChem*, 2017, **10**, 4465.
85 W. Shao, M. Li, X. Wang, N. Fu and Z. Yang, *J. Alloys Compd.*, 2022, **929**, 167141.
86 T. Mushove, T. M. Breault and L. T. Thompson, *Ind. Eng. Chem. Res.*, 2015, **54**, 4285.
87 M. Mohiuddin, A. Zavabeti, F. Haque, A. Mahmood, R. S. Datta, N. Syed, M. W. Khan, A. Jannat, K. Messalea, B. Y. Zhang, G. Chen, H. Zhang, J. Z. Ou and N. Mahmood, *J. Mater. Chem. A*, 2020, **8**, 2789.
88 X. Lu, Y. Zeng, M. Yu, T. Zhai, C. Liang, S. Xie, M.-S. Balogun and Y. Tong, *Adv. Mater.*, 2014, **26**, 3148.
89 Y. Chen, C. Kang, L. Ma, L. Fu, G. Li, Q. Hu and Q. Liu, *Chem. Eng. J.*, 2021, **417**, 129243.
90 D. O. B. Apriandanu, S. Nomura, S. Nakayama, C. Tateishi and F. Amano, *Catal. Today*, 2022, DOI: **10.1016/j.cattod.2022.06.041**.
91 A. Puthirath Balan, S. Radhakrishnan, C. F. Woellner, S. K. Sinha, L. Deng, C. de los Reyes, B. M. Rao, M. Paulose, R. Neupane, A. Apte, V. Kochat, R. Vajtai, A. R. Harutyunyan, C.-W. Chu, G. Costin, D. S. Galvao, A. A. Martí, P. A. van Aken, O. K. Varghese, C. S. Tiwary, A. Malie Madom Ramaswamy Iyer and P. M. Ajayan, *Nat. Nanotechnol.*, 2018, **13**, 602.
92 S. Han, L. Hu, Z. Liang, S. Wageh, A. A. Al-Ghamdi, Y. Chen and X. Fang, *Adv. Funct. Mater.*, 2014, **24**, 5719.
93 L. Yue, S. Zhang, H. Zhao, M. Wang, J. Mi, Y. Feng and D. Wang, *J. Alloys Compd.*, 2018, **765**, 1263.
94 X. Lv, S. Shao, Y. Xiao and J. Deng, *Appl. Surf. Sci.*, 2021, **560**, 150036.
95 Z. Zhou, Q. Zhang, J. Sun, B. He, J. Guo, Q. Li, C. Li, L. Xie and Y. Yao, *ACS Nano*, 2018, **12**, 9333.
96 J. Y. Lu, Y. R. Yuan, X. Hu, W. J. Liu, C. X. Li, H. Q. Liu and W. W. Li, *Ind. Eng. Chem. Res.*, 2020, **59**, 1800.
97 J. Shamsi, A. S. Urban, M. Imran, L. De Trizio and L. Manna, *Chem. Rev.*, 2019, **119**, 3296.
98 V. Valtchev, G. Majano, S. Mintova and J. Pérez-Ramírez, *Chem. Soc. Rev.*, 2013, **42**, 263.
99 Z. Li, S. Dai, L. Ma, Z. Qu, N. Yan and J. Li, *Chem. Eng. J.*, 2021, **413**, 127447.
100 R. Gao, J. Wang, Z.-F. Huang, R. Zhang, W. Wang, L. Pan, J. Zhang, W. Zhu, X. Zhang, C. Shi, J. Lim and J.-J. Zou, *Nat. Energy*, 2021, **6**, 614.
101 H. Fu, Y. Guo, J. Yu, Z. Shen, J. Zhao, Y. Xie, Y. Ling, S. Ouyang, S. Li and W. Zhang, *Chin. Chem. Lett.*, 2021, **33**, 957–962.
102 X. Fan, T. Wang, H. Xue, B. Gao, S. Zhang, H. Gong, H. Guo, L. Song, W. Xia and J. He, *ChemElectroChem*, 2019, **6**, 543.
103 H. Fan, K. Mao, M. Liu, O. Zhuo, J. Zhao, T. Sun, Y. Jiang, X. Du, X. Zhang, Q. Wu, R. Che, L. Yang, Q. Wu, X. Wang and Z. Hu, *J. Mater. Chem. A*, 2018, **6**, 21313.
104 Z. W. Seh, J. Kibsgaard, C. F. Dickens, I. Chorkendorff, J. K. Nørskov and T. F. Jaramillo, *Science*, 2017, **355**, eaad4998.
105 H. Zhang, P. Li, H. Zhou, J. Xu, Q. Jiang, J. H. L. Hadden, Y. Wang, M. Wang, S. Chen, F. Xie and D. J. Riley, *Nano Energy*, 2022, **94**, 106968.

106 W. L. Kwong, C. C. Lee, A. Shchukarev and J. Messinger, *Chem. Commun.*, 2019, **55**, 5017.
107 H. C. Nguyën, F. A. Garcés-Pineda, M. de Fez-Febré, J. R. Galán-Mascarós and N. López, *Chem. Sci.*, 2020, **11**, 2464.
108 H. Wu, T. Yang, Y. Du, L. Shen and G. W. Ho, *Adv. Mater.*, 2018, **30**, 1804341.
109 T. Takashima, S. Hemmi, Q. Liu and H. Irie, *Catal. Sci. Technol.*, 2020, **10**, 3748.
110 Z. Zhang, D. Zhou, X. Bao, G. Huang and B. Huang, *Int. J. Hydrogen Energy*, 2019, **44**, 2877.
111 R. N. Ali, H. Naz, X. Zhu, J. Xiang, G. Hu and B. Xiang, *Mater. Res. Express*, 2018, **6**, 025516.
112 D. Zhu, C. Guo, J. Liu, L. Wang, Y. Du and S.-Z. Qiao, *Chem. Commun.*, 2017, **53**, 10906.
113 M. Zeng, J. Wu, Z. Li, H. Wu, J. Wang, H. Wang, L. He and X. Yang, *ACS Sustainable Chem. Eng.*, 2019, **7**, 4777.
114 S. Ni, H. Qu, Z. Xu, X. Zhu, H. Xing, L. Wang, J. Yu, H. Liu, C. Chen and L. Yang, *Appl. Catal., B*, 2021, **299**, 120638.
115 M. Ranjani, N. Senthilkumar, G. G. Kumar and A. Manthiram, *J. Mater. Chem. A*, 2018, **6**, 23019.
116 G. Ma, Q. Xue, J. Zhu, X. Zhang, X. Wang, H. Yao, G. Zhou and Y. Chen, *Appl. Catal., B*, 2020, **265**, 118567.
117 Y. Ding, Y. Li, Y. Xue, B. Miao, S. Li, Y. Jiang, X. Liu and Y. Chen, *Nanoscale*, 2019, **11**, 1058.
118 W. Yang, X. Yang, C. Hou, B. Li, H. Gao, J. Lin and X. Luo, *Appl. Catal., B*, 2019, **259**, 118020.
119 G. Das, R. M. Tesfaye, Y. Won and H. H. Yoon, *Electrochim. Acta*, 2017, **237**, 171.
120 B. Ma, H. Zhao, T. Li, Q. Liu, Y. Luo, C. Li, S. Lu, A. M. Asiri, D. Ma and X. Sun, *Nano Res.*, 2021, **14**, 555.
121 V. Kyriakou, I. Garagounis, A. Vourros, E. Vasileiou and M. Stoukides, *Joule*, 2020, **4**, 142.
122 S. Chen, S. Perathoner, C. Ampelli, C. Mebrahtu, D. Su and G. Centi, *Angew. Chem., Int. Ed.*, 2017, **56**, 2699.
123 Y. Yao, S. Zhu, H. Wang, H. Li and M. Shao, *J. Am. Chem. Soc.*, 2018, **140**, 1496.
124 C. Choi, S. Back, N.-Y. Kim, J. Lim, Y.-H. Kim and Y. Jung, *ACS Catal.*, 2018, **8**, 7517.
125 C. Zhang, S. Liu, T. Chen, Z. Li and J. Hao, *Chem. Commun.*, 2019, **55**, 7370.
126 S. Yu, Q. Wang, J. Wang, Y. Xiang, X. Niu and T. Li, *Int. J. Hydrogen Energy*, 2021, **46**, 14331.
127 H. Wan, X. Liu, H. Wang, R. Ma and T. Sasaki, *Nanoscale Horiz.*, 2019, **4**, 789.
128 H. Wan, F. Chen, W. Ma, X. Liu and R. Ma, *Nanoscale*, 2020, **12**, 21479.
129 X. Huang, T. Shen, T. Zhang, H. Qiu, X. Gu, Z. Ali and Y. Hou, *Adv. Energy Mater.*, 2020, **9**, 1900375.
130 H. Wan, M. Lv, X. Liu, G. Chen, N. Zhang, Y. Cao, H. Wang, R. Ma and G. Qiu, *ACS Sustainable Chem. Eng.*, 2019, **7**, 11841.
131 K. Maiti, N. H. Kim and J. H. Lee, *Chem. Eng. J.*, 2021, **410**, 128358.
132 S. C. Perry, D. Pangotra, L. Vieira, L.-I. Csepei, V. Sieber, L. Wang, C. Ponce de León and F. C. Walsh, *Nat. Rev. Chem.*, 2019, **3**, 442.
133 R. Gao, L. Pan, Z. Li, C. Shi, Y. Yao, X. Zhang and J. Zou, *Adv. Funct. Mater.*, 2020, **30**, 1910539.
134 X. Cheng, S. Dou, G. Qin, B. Wang, P. Yan, T. T. Isimjan and X. Yang, *Int. J. Hydrogen Energy*, 2020, **45**, 6128.
135 M. Kou, W. Liu, Y. Wang, J. Huang, Y. Chen, Y. Zhou, Y. Chen, M. Ma, K. Lei, H. Xie, P. K. Wong and L. Ye, *Appl. Catal., B*, 2021, **291**, 120146.
136 J. Albero, Y. Peng and H. García, *ACS Catal.*, 2020, **10**, 5734.
137 Y. Zhao, L. Zheng, R. Shi, S. Zhang, X. Bian, F. Wu, X. Cao, G. I. N. Waterhouse and T. Zhang, *Adv. Energy Mater.*, 2020, **10**, 2002199.
138 G. Zhang, Z.-A. Lan and X. Wang, *Angew. Chem., Int. Ed.*, 2016, **55**, 15712.
139 S. R. Pendlebury, A. J. Cowan, M. Barroso, K. Sivula, J. Ye, M. Grätzel, D. R. Klug, J. Tang and J. R. Durrant, *Energy Environ. Sci.*, 2012, **5**, 6304.
140 H. J. Ahn, M. J. Kwak, J. S. Lee, K. Y. Yoon and J. H. Jang, *J. Mater. Chem. A*, 2014, **2**, 19999.
141 A. T. Paradzah, K. D. Maabong, H. M. A. M. Elnour, A. Singh, M. Diale and T. P. J. Krüger, *J. Phys. Chem. C*, 2019, **123**, 18676.
142 G. Zhang, Z. Wang and J. Wu, *Nanoscale*, 2021, **13**, 4359.
143 R. Mazzaro, S. Boscolo Bibi, M. Natali, G. Bergamini, V. Morandi, P. Ceroni and A. Vomiero, *Nano Energy*, 2019, **61**, 36.
144 Z. Jiang, W. Wan, H. Li, S. Yuan, H. Zhao and P. K. Wong, *Adv. Mater.*, 2018, **30**, 1706108.
145 Y. Jia, W. Zhang, J. Yeon Do, M. Kang and C. Liu, *Chem. Eng. J.*, 2020, **402**, 126193.
146 Z. Mu, S. Chen, Y. Wang, Z. Zhang, Z. Li, B. Xin and L. Jing, *Small Sci.*, 2021, **1**, 2100050.
147 Y. Jiang, J.-F. Liao, H.-Y. Chen, H.-H. Zhang, J.-Y. Li, X.-D. Wang and D.-B. Kuang, *Chem*, 2020, **6**, 766.
148 M. Padervand, B. Rhimi and C. Wang, *J. Alloys Compd.*, 2021, **852**, 156955.
149 H. Guo, M. Chen, Q. Zhong, Y. Wang, W. Ma and J. Ding, *J. CO_2 Util.*, 2019, **33**, 233.
150 N. Kumar, N. Seriani and R. Gebauer, *Phys. Chem. Chem. Phys.*, 2020, **22**, 10819.
151 S. Liu, S. Wang, Y. Jiang, Z. Zhao, G. Jiang and Z. Sun, *Chem. Eng. J.*, 2019, **373**, 572.
152 W. Zhang, D. Han, M. Dai, Y. Fan, G. Pan, W. Liang, Q. Zheng, D. Qin, D. Han, Y. He and L. Niu, *ACS Sustainable Chem. Eng.*, 2021, **9**, 15331.
153 G. Zhang and X. Wang, *Angew. Chem., Int. Ed.*, 2019, **58**, 15580.
154 L. Wang, Y. Zhang, L. Chen, H. Xu and Y. Xiong, *Adv. Mater.*, 2018, **30**, 1801955.
155 Y. Fang, X. Fu and X. Wang, *ACS Mater. Lett.*, 2020, **2**, 975.
156 Z. Pan, G. Zhang and X. Wang, *Angew. Chem.*, 2019, **131**, 7176.
157 M. Wang, D. Li, Y. Zhao, H. Shen, B. Chen, X. Wu, X. Qiao and W. Shi, *Catal. Sci. Technol.*, 2021, **11**, 681.
158 A. Fujishima and K. Honda, *Nature*, 1972, **238**, 37.
159 J. Wang, C. Du, Q. Peng, J. Yang, Y. Wen, B. Shan and R. Chen, *Int. J. Hydrogen Energy*, 2017, **42**, 29140.

160 Z. Sun, G. Fang, J. Li, J. Mo, X. He, X. Wang and Z. Yu, *Chem. Phys. Lett.*, 2020, **754**, 137736.
161 R. Zhang, Y. Fang, T. Chen, F. Qu, Z. Liu, G. Du, A. M. Asiri, T. Gao and X. Sun, *ACS Sustainable Chem. Eng.*, 2017, **5**, 7502.
162 A. Liu, Y. Zhang, W. Ma, W. Song, C. Chen and J. Zhao, *J. Photochem. Photobiol., A*, 2018, **355**, 290.
163 P. Zhang, L. Yu and X. W. D. Lou, *Angew. Chem., Int. Ed.*, 2018, **57**, 15076.
164 Z. Zhang, H. Nagashima and T. Tachikawa, *Angew. Chem., Int. Ed.*, 2020, **59**, 9047.
165 S. Hu, L. Jiang, B. Wang and Y. Ma, *Int. J. Hydrogen Energy*, 2019, **44**, 13214.
166 S. Adhikari, S. Selvaraj and D.-H. Kim, *Appl. Catal., B*, 2019, **244**, 11.
167 P. Kassal, M. D. Steinberg and I. M. Steinberg, *Sens. Actuators, B*, 2018, **266**, 228.
168 E. Lee, Y. S. Yoon and D.-J. Kim, *ACS Sens.*, 2018, **3**, 2045.
169 K. Movlaee, M. Ganjali, P. Norouzi and G. Neri, *Nanomaterials*, 2017, **7**, 406.
170 D. Tyagi, H. Wang, W. Huang, L. Hu, Y. Tang, Z. Guo, Z. Ouyang and H. Zhang, *Nanoscale*, 2020, **12**, 3535.
171 A. Umar, A. A. Ibrahim, R. Kumar, H. Albargi, M. A. Alsaiari and F. Ahmed, *Sens. Actuators, B*, 2021, **326**, 128851.
172 D. Zhang, M. Chen, H. Zou, Y. Zhang, J. Hu, H. Wang, B. Zi, J. Zhang, Z. Zhu, L. Duan and Q. Liu, *Nanotechnology*, 2020, **31**, 215601.
173 X. Wang, T. Wang, G. Si, Y. Li, S. Zhang, X. Deng and X. Xu, *Sens. Actuators, B*, 2020, **302**, 127165.
174 P. Wolkoff and G. D. Nielsen, *Atmos. Environ.*, 2001, **35**, 4407.
175 E. Woolfenden, *J. Chromatogr. A*, 2010, **1217**, 2685.
176 G. Lube and M. Goodarzi, *J. Pharm. Biomed. Anal.*, 2018, **147**, 313.
177 J. Xu, J. Han, Y. Zhang, Y. Sun and B. Xie, *Sens. Actuators, B*, 2008, **132**, 334.
178 H.-J. Kim and J.-H. Lee, *Sens. Actuators, B*, 2014, **192**, 607.
179 H. Ji, W. Zeng and Y. Li, *Nanoscale*, 2019, **11**, 22664.
180 J. Cao, Z. Wang, R. Wang, S. Liu, T. Fei, L. Wang and T. Zhang, *J. Mater. Chem. A*, 2015, **3**, 5635.
181 C. Wang, X. Cheng, X. Zhou, P. Sun, X. Hu, K. Shimanoe, G. Lu and N. Yamazoe, *ACS Appl. Mater. Interfaces*, 2014, **6**, 12031.
182 J. M. Suh, Y.-S. Shim, D. H. Kim, W. Sohn, Y. Jung, S. Y. Lee, S. Choi, Y. H. Kim, J.-M. Jeon, K. Hong, K. C. Kwon, S. Y. Park, C. Kim, J.-H. Lee, C.-Y. Kang and H. W. Jang, *Adv. Mater. Technol.*, 2017, **2**, 1600259.
183 D. H. Kim, T. H. Kim, W. Sohn, J. M. Suh, Y.-S. Shim, K. C. Kwon, K. Hong, S. Choi, H.-G. Byun, J.-H. Lee and H. W. Jang, *Sens. Actuators, B*, 2018, **274**, 587.
184 X. Zhang, Y. Liu, H. Liu, T. Liang, P. Zhang and Z. Dai, *Sens. Actuators, B*, 2021, **345**, 130357.
185 F. C. O. L. Martins, M. A. Sentanin and D. De Souza, *Food Chem.*, 2019, **272**, 732.
186 M. Carocho, M. F. Barreiro, P. Morales and I. C. F. R. Ferreira, *Compr. Rev. Food Sci. Food Saf.*, 2014, **13**, 377.
187 Z. Kalaycıoğlu and F. B. Erim, *J. Agric. Food Chem.*, 2019, **67**, 7205.
188 M. Harvey, G. Cave and G. Chanwai, *Emerg. Med. Australas.*, 2010, **22**, 463.
189 S. Wang, M. Liu, S. He, S. Zhang, X. Lv, H. Song, J. Han and D. Chen, *Sens. Actuators, B*, 2018, **260**, 490.
190 J. Schullehner, L. Stayner and B. Hansen, *Int. J. Environ. Res. Public Health*, 2017, **14**, 276.
191 N. G. Hord, J. S. Ghannam, H. K. Garg, P. D. Berens and N. S. Bryan, *Breastfeed. Med.*, 2011, **6**, 393.
192 C. Jin and A. Yonezawa, *Pharmacol. Ther.*, 2022, **233**, 108023.
193 Z. Aminov and D. O. Carpenter, *Environ. Pollut.*, 2020, **260**, 114004.
194 S. G. Mallat, S. Al Kattar, B. Y. Tanios and A. Jurjus, *Curr. Hypertens. Rep.*, 2016, **18**, 74.
195 S. Meenakshi, S. Anitta, A. Sivakumar, S. A. Martin Britto Dhas and C. Sekar, *Microchem. J.*, 2021, **168**, 106403.
196 L. Xia, X. Li, F. Zhu, S. Hu and L. Huang, *J. Phys. Chem. C*, 2017, **121**, 20279.
197 Y. A. Nor, L. Zhou, A. K. Meka, C. Xu, Y. Niu, H. Zhang, N. Mitter, D. Mahony and C. Yu, *Adv. Funct. Mater.*, 2016, **26**, 5408.
198 S. Naz, M. Islam, S. Tabassum, N. F. Fernandes, E. J. Carcache de Blanco and M. Zia, *J. Mol. Struct.*, 2019, **1185**, 1.
199 W. Zhao, H. Chen, Y. Li, L. Li, M. Lang and J. Shi, *Adv. Funct. Mater.*, 2008, **18**, 2780.
200 Y. Lu, L. Zhang, J. Li, Y.-D. Su, Y. Liu, Y.-J. Xu, L. Dong, H.-L. Gao, J. Lin, N. Man, P.-F. Wei, W.-P. Xu, S.-H. Yu and L.-P. Wen, *Adv. Funct. Mater.*, 2013, **23**, 1534.
201 N. Lee and T. Hyeon, *Chem. Soc. Rev.*, 2012, **41**, 2575.
202 J. Xu, R. Shi, G. Chen, S. Dong, P. Yang, Z. Zhang, N. Niu, S. Gai, F. He, Y. Fu and J. Lin, *ACS Nano*, 2020, **14**, 9613–9625.
203 D. Shahbazi-Gahrouei, M. Williams, S. Rizvi and B. J. Allen, *J. Magn. Reson. Imaging*, 2001, **14**, 169.
204 W. Ren, G. Tian, L. Zhou, W. Yin, L. Yan, S. Jin, Y. Zu, S. Li, Z. Gu and Y. Zhao, *Nanoscale*, 2012, **4**, 3754.
205 S. Rodriguez-Liviano, A. I. Becerro, D. Alcántara, V. Grazú, J. M. de la Fuente and M. Ocaña, *Inorg. Chem.*, 2013, **52**, 647.
206 F. Wang, E. Peng, B. Zheng, S. F. Y. Li and J. M. Xue, *J. Phys. Chem. C*, 2015, **119**, 23735.
207 Y. Shao, X. Tian, W. Hu, Y. Zhang, H. Liu, H. He, Y. Shen, F. Xie and L. Li, *Biomaterials*, 2012, **33**, 6438.
208 S. R. Dave and X. Gao, *Wiley Interdiscip. Rev.: Nanomed. Nanobiotechnol.*, 2009, **1**, 583.
209 H. Wan, P. Rong, X. Liu, L. Yang, Y. Jiang, N. Zhang, R. Ma, S. Liang, H. Wang and G. Qiu, *Adv. Funct. Mater.*, 2017, **27**, 1606821.
210 S. Marasini, H. Yue, S. L. Ho, K.-H. Jung, J. A. Park, H. Cha, A. Ghazanfari, M. Y. Ahmad, S. Liu, Y. J. Jang, X. Miao, K.-S. Chae, Y. Chang and G. H. Lee, *Eur. J. Inorg. Chem.*, 2019, **2019**, 3832.
211 V. Calcagno, R. Vecchione, V. Quagliariello, P. Marzola, A. Busato, P. Giustetto, M. Profeta, S. Gargiulo,

C. D. Cicco, H. Yu, M. Cassani, N. Maurea, M. Mancini, T. Pellegrino and P. A. Netti, *Adv. Healthcare Mater.*, 2019, **8**, 1801313.

212 V. Gómez-Vallejo, M. Puigivila, S. Plaza-García, B. Szczupak, R. Piñol, J. L. Murillo, V. Sorribas, G. Lou, S. Veintemillas, P. Ramos-Cabrer, J. Llop and A. Millán, *Nanoscale*, 2018, **10**, 14153.

213 A. Meddahi-Pellé, A. Legrand, A. Marcellan, L. Louedec, D. Letourneur and L. Leibler, *Angew. Chem., Int. Ed.*, 2014, **53**, 6369.

214 M. Long, Y. Zhang, P. Huang, S. Chang, Y. Hu, Q. Yang, L. Mao and H. Yang, *Adv. Funct. Mater.*, 2018, **28**, 1704452.

215 B. Engelmann and S. Massberg, *Nat. Rev. Immunol.*, 2013, **13**, 34.